

# Shallow cirrus convection – a source for ice supersaturation

By PETER SPICHTINGER\*, *Institute for Atmospheric Physics, Johannes Gutenberg University, Mainz, Germany*

(Manuscript received 23 October 2012; in final form 21 July 2014)

## ABSTRACT

The origin and persistence of high ice supersaturation is still not well understood. In this study, the impact of local dynamics as source for ice supersaturation inside cirrus clouds is investigated. Nucleation and growth of ice crystals inside potentially unstable layers in the tropopause region might lead to shallow convection inside (layered) cirrus clouds due to latent heat release. The intrinsic updraught inside convective cells constitutes a dominant but transient source for ice supersaturation. A realistic case of shallow cirrus convection is investigated using radiosonde data, meteorological analyses and large-eddy simulations of cirrus clouds. The simulations corroborate the existence of ice supersaturation inside cirrus clouds as a transient phenomenon. Ice supersaturation is frequent, but determined by the life cycle of convective cells in shallow cirrus convection. Cirrus clouds driven by shallow cirrus convection are mostly not in thermodynamic equilibrium; they are usually in a subsaturated or supersaturated state.

*Keywords:* cirrus clouds, ice supersaturation, cloud dynamics, thermodynamics

## 1. Introduction

Pure ice clouds, so-called cirrus clouds, in the tropopause region are still not well understood. Their net radiative impact on Earth's energy budget is uncertain; a net warming is often assumed (Chen et al., 2000) but not confirmed yet. Microphysical properties of cirrus clouds might lead to transitions between net cooling and warming (see e.g. Zhang et al., 1999; Fusina et al., 2007). Macrophysical cloud inhomogeneities additionally influence radiative transfer inside cirrus clouds. Beneath the uncertain radiative impact of cirrus clouds, their internal structure is also quite unknown and bears some unknown issues (Peter et al., 2006). During the last years, many *in situ* measurements (airborne or from balloon records) show high ice supersaturation inside cirrus clouds, that is, values of supersaturation ratio  $S_i \geq 1.2$  (see, e.g. Krämer et al., 2009). Since ice formation takes place far away from thermodynamic equilibrium (i.e. at supersaturations  $S_i \geq 1.2$ , see, e.g., Koop et al., 2000; DeMott et al., 2003) cloud-free air masses can exist in the state of ice supersaturation for quite a long time. Many measurements

in the tropopause region indicate these so-called ice-supersaturated regions (ISSRs, see, e.g. Gierens et al., 1999), which can reach quite large horizontal extensions from hundreds to thousands of kilometres (Gierens and Spichtinger, 2000). Ice supersaturation in clear air was found in many measurement campaigns using a variety of different measurement techniques (Jensen et al., 1998; Ovarlez et al., 2000; Vay et al., 2000; Haag et al., 2003; Krämer et al., 2009) as well as in satellite observations (Spichtinger et al., 2003b; Gierens et al., 2004; Gettelman et al., 2006). The frequency of occurrence of ice supersaturation inside cirrus clouds seems to be very high, since many measurement points can be found far from saturation (see, e.g. Fig. 3 in Krämer et al., 2009). Thus, one tends to think that (high) ice supersaturation might also persist for a long time (see discussion in Peter et al., 2006). Persistent high ice supersaturation inside (thick) cirrus clouds seems to be in contrast to our current understanding.<sup>1</sup> Ice crystals should act as strong sink for ice supersaturation, and without any additional forcing the cloud should relax to thermodynamic

\*Correspondence.

email: spichtin@uni-mainz.de

Responsible Editor: Abdel Hannachi, Stockholm University, Sweden.

<sup>1</sup>Note that in most discussions, no definitions on 'high supersaturation' and 'thick cirrus clouds' are given. There is a kind of common sense on high values (usually  $S_i > 1.3$ , close to nucleation thresholds), but clear definitions are lacking.

equilibrium (i.e. saturation) quite fast due to diffusional growth. For explaining the issue of high and (probably) persistent ice supersaturation inside cirrus clouds, many different mechanisms were proposed. Here, we summarise some of the most probable effects.

- It is quite difficult to measure water vapour at low temperatures with high precision. Recent inter-comparisons of state-of-the-art *in situ* measurement techniques indicated errors in the range up to about 10% in the temperature regime with  $T > 193$  K; in the low temperature range ( $T < 193$  K), higher relative errors and also systematical biases can occur (see comparison in Fahey et al., 2014).
- Pure water does not exist at temperatures  $T < 233$  K. However, for calculating water activity as a key quantity for nucleation rates (Koop et al., 2000) or for converting standard meteorological measurements (reported in relative humidity over liquid water), the saturation vapour pressure over liquid water is necessary. As Murphy and Koop (2005) have pointed out in their review, many saturation pressure extrapolations have large errors. Even by using thermodynamical constraints for best estimates, relative errors in the range up to 10% might occur. Saturation vapour pressure over solid ice is much better constrained by measurements, and variations between different formulae are in the range of 2%.
- Cubic ice as meta stable phase was assumed in lab and field measurements (Murphy, 2003; Murray et al., 2005; Shilling et al., 2006; Murray, 2008b). Since its saturation water vapour pressure is higher than the saturation pressure over hexagonal ice, hexagonal ice crystals will grow on the expense of cubic ice crystals. The transformation timescale (cubic  $\rightarrow$  hexagonal ice) increases with decreasing temperature. At low temperatures, high ice supersaturation might arise from the dominance of cubic ice particles, which are actually in thermodynamic equilibrium with gas phase.
- The mass accommodation coefficient for water vapour uptake of ice crystals is still uncertain. Measurements show a large variability in the range  $0.004 \leq \alpha \leq 1.06$  (see Skrotzki et al., 2013, for a recent review). Very small values ( $\alpha \ll 0.1$ ) would lead to weaker diffusional growth and in turn to slower relaxation of humidity to thermodynamic equilibrium. On the other hand, strongly reduced growth would lead to tremendously high ice crystal number concentrations some orders of magnitude higher than observed (see, e.g. Kay and Wood, 2008).

- Laboratory experiments show inhibition of homogeneous nucleation in aqueous solution droplets contaminated with a high amount of organic substances due to a size reduction (Kärcher and Koop, 2005). This effect could lead to reduction in ice crystal number concentrations and in turn to high ice supersaturation inside cirrus clouds due to reduced diffusional growth.
- Laboratory experiments show transition to glassy states for several organic compounds (Murray, 2008a; Zobrist et al., 2008; Murray et al., 2010; Koop et al., 2011). Thus, homogeneous nucleation could be inhibited and higher ice supersaturation could occur.
- Coating of solution droplets might also inhibit ice formation, thus leading to high ice supersaturation. Also, this feature was found in laboratory experiments (Bogdan and Molina, 2009).

Most of these suggested explanations are based on special and complex microphysical effects found in laboratory experiments. There is only slight evidence from *in situ* measurements on the representativity of these effects in real atmosphere. For instance, it is not clear how many organic compounds occur in the upper troposphere, if they are the ‘right’ ones and if their concentration is high enough for inhibiting ice formation. Almost all aerosol particles must be contaminated in order to suppress homogeneous nucleation (see discussion in Kärcher and Koop, 2005). Most of the listed effects are just important for the low temperature regime ( $T < 200$  K). However, in the warm regime ( $200 \leq T \leq 235$  K) high ice supersaturation inside cirrus clouds occurs as well (Krämer et al., 2009). In most discussions, the impact of local dynamics is missing, but dynamics play a crucial role as can be seen clearly in relative humidity rates in a simple parcel approach. Relative humidity over ice is defined as follows

$$RH_i = 100\% S_i = 100\% \frac{p \cdot q}{\epsilon \cdot p_{ice}(T)} \quad (1)$$

with pressure  $p$ , temperature  $T$ , specific humidity or water vapour mixing ratio  $q$ , saturation pressure over ice  $p_{ice}(T)$  and ratio of molar masses of water vapour and air  $\epsilon = \frac{M_{mol,H_2O}}{M_{mol,air}}$ , respectively. The total derivative of relative humidity over ice can be determined as follows:

$$\begin{aligned} \frac{dRH_i}{dt} &= \frac{\partial RH_i}{\partial T} \frac{dT}{dt} + \frac{\partial RH_i}{\partial p} \frac{dp}{dt} + \frac{\partial RH_i}{\partial q} \frac{dq}{dt} \quad (2) \\ &= \frac{RH_i}{T} \left[ \frac{L_s}{R_v T} - \frac{1}{\kappa} \right] \cdot \frac{g}{c_p} w \\ &\quad + RH_i \left[ \frac{L_s^2}{R_v T^2 c_p} + \frac{1}{q} \right] \frac{dq}{dt} \Big|_{phase} + \frac{RH_i}{q} \frac{dq}{dt} \Big|_{mix} \quad (3) \end{aligned}$$

Here,  $L_s$  denotes latent heat of sublimation,  $c_p$  is the specific heat capacity of dry air,  $R, R_v$  are specific ideal gas constants for dry air and water vapour, respectively, with  $\kappa = \frac{R}{c_p}$  and  $g$  denotes gravity acceleration of Earth. Equation (3) is derived in the Appendix. We assume adiabatic processes, that is, no heat exchange with ambient air is possible; thus, vertical motions lead to expansion or compression and in turn to temperature changes of air. Equation (3) can be separated into a part driven by vertical motions (i.e. dynamics), a part governed by diffusional growth of existing ice crystals ( $\frac{dq_c}{dt} = -\frac{dq}{dt}|_{phase}$ ) and a part driven by mixing. For upward motions, the first term constitutes a source for supersaturation whereas in cloudy air ice mass acts as a sink for ice supersaturation (second term). If we only consider (constant) cooling and diffusional growth, neglecting all other processes, the system will relax to a quasi-equilibrium state at  $S_i > 1$  (Korolev and Mazin, 2003).

The majority of measurements inside cirrus clouds indicates that these clouds are **not** in thermodynamic equilibrium (i.e. saturation) or even in a quasi-steady state; the internal variability of (bulk) microphysical properties (ice crystal number concentrations, ice water content) and of thermodynamic properties (temperature, pressure) is very high, leading to a ‘patchiness’ of cirrus clouds (see, e.g. Lee et al., 2004; Krämer et al., 2009). One main reason for this behaviour is the dynamic nature of the atmosphere.

Cirrus clouds are part of a multi-scale system characterised by a superposition of many different motions on different scales. The main driver for stratiform cirrus clouds in mid-latitudes is probably synoptic-scale dynamics, which triggers slow upward motions (e.g. Spichtinger et al., 2005a). Mesoscale dynamics (e.g. gravity waves) can be superimposed on large-scale dynamics. Important sources for tropospheric gravity waves are topography (Smith, 1979; Jensen et al., 1998; Joos et al., 2008, 2009), convection (Bretherton and Smolarkiewicz, 1989; Lane et al., 2001), baroclinic instabilities and frontal activities (Lane et al., 2004; Plougonven et al., 2005), geostrophic adjustment (Plougonven et al., 2003; Spichtinger et al., 2005b), spontaneous imbalance (O’Sullivan and Dunkerton, 1995) and wind shear (Rosenthal and Lindzen, 1983; Lott et al., 1992), respectively. Small-scale motions as turbulence could be additionally superimposed on large-scale and mesoscale dynamics. Turbulence is strongly connected to wave activity and breaking waves (McIntyre, 2008).

Partly, the impact of mesoscale dynamics in terms of ‘temperature fluctuations’ (see, e.g. Gary, 2006) was investigated by using Lagrangian box models (e.g. Haag and Kärcher, 2004; Hoyle et al., 2005; Kay et al., 2006, 2007; Gensch et al., 2008; Brabec et al., 2013; Cirisan et al., 2013) or single column models (e.g. Comstock et al., 2008; Cirisan

et al., 2014), respectively. However, the question arises if such investigations are biased because variations are prescribed in a very rigorous way. Cloud processes have to react on the temperature changes without any possibility to rearrange the vertical updraughts spatially. Additional horizontal dimensions will change cloud evolution crucially. Spichtinger and Gierens (2009a, 2009b, 2009c) could show that even weak small-scale dynamics can influence the formation and evolution of cirrus clouds in both directions. The amount of ice crystals produced in homogeneous freezing events might be enhanced by larger vertical velocities. Horizontally spread ice crystals could quench nucleation events. An important feature for these different effects is an organisation of temperature variations in interactions with environmental wind fields (see Figs. 13 and 16 in Spichtinger and Gierens, 2009b).

However, sources of these motions and their interactions with cirrus clouds in more than one spatial direction were only marginally investigated. The classical view of cloud dynamics with convective cell formation due to latent heat release (e.g. Houze, 1993; Lin, 2008) is generally missing, although there are some investigations into this directions (e.g. Marsham and Dobbie, 2005).

In this study, we focus on shallow convection in ice-supersaturated layers and cirrus clouds as a source for ice supersaturation inside cirrus clouds. The study follows the classical composition: In the next section, the model for investigating cirrus clouds and their interaction with mesoscale dynamics is described briefly. In Section 3, a real case of a potential unstable layer in the upper troposphere is presented; we show results from simulations corroborating ice supersaturation inside (thick) cirrus clouds. In Section 4, some additional effects possibly affecting the results are discussed. Finally, in Section 5 general findings are summarised and an outlook to further applications of this kind of investigations is given.

## 2. Model description

In the following, the cirrus cloud model is described briefly. For a detailed description of the dynamical model we refer to Smolarkiewicz and Margolin (1997) or Prusa et al. (2008); for a detailed description of the ice microphysics we refer to Spichtinger and Gierens (2009a).

The anelastic, non-hydrostatic model Eulag (Prusa et al., 2008) is used in this study. For representing ice clouds, a two-moment bulk microphysics scheme is used as described by Spichtinger and Gierens, 2009a. This model version (Eulag+ice microphysics) was already used for investigations of the impact of dynamics and aerosols on the formation and evolution of cirrus clouds (Joos et al., 2009, 2014; Spichtinger and Gierens, 2009b, 2009c; Fusina and

Spichtinger, 2010). The scheme includes the following processes: Ice crystal nucleation (homogeneous/heterogeneous), diffusional growth/sublimation and sedimentation. Arbitrary many classes of ice can be treated, discriminated by their formation mechanism (e.g. homogeneous freezing of aqueous solution droplets or heterogeneous nucleation on different aerosol types, see, e.g., Spichtinger and Gierens, 2009b, 2009c; Spichtinger and Cziczo, 2010). An ice class is represented by four variables, that is, ice crystal mass concentration, ice crystal number concentration, background aerosol mass concentration and background aerosol number concentration, respectively. The ice crystal mass is distributed according to a lognormal distribution with variable modal mass but fixed width (i.e. geometric standard deviation  $\sigma_m = 2.85$ ). The background aerosol is connected to ice crystal nucleation in a one-to-one way, that is, washout of aerosols and release after crystal sublimation is possible. In this study, mostly one class of ice is used, representing homogeneous freezing of aqueous solution droplets. We assume that this mechanism constitutes the dominant nucleation process in the upper troposphere (e.g. Kärcher and Ström, 2003). Nucleation rates are parameterised according to Koop et al. (2000), using water activity and temperature as key variables. Sulphuric acid is used as background aerosol; the ‘dry’ acid droplets are log-normally distributed with a modal radius of  $r_d = 25$  nm and a geometric standard deviation of  $\sigma_r = 1.4$ . These parameters are used according to the findings in Spichtinger and Gierens (2009a). The total background concentration of sulphuric acid droplets is  $n_d = 300$  cm<sup>-3</sup>, as thought to be a typical value for upper tropospheric conditions (Minikin et al., 2003). Heterogeneous nucleation might modulate homogeneous nucleation, but in mid-latitudes ice nuclei (IN) concentrations are usually quite low, leading to small changes. For sensitivity studies (see discussion in Section 4) heterogeneous nucleation was used. We use a second ice class; heterogeneous ice formation was parameterised by a threshold condition. If  $RHi$  surpasses a threshold  $RHi_{het,thres} = 130\%$ , all available IN (i.e. aerosol particles of the assigned ice class) are transformed to ice crystals. We prescribe a number concentration  $N_{IN} = 10$  L<sup>-1</sup> (DeMott et al., 2003), typical for extra-tropical upper tropospheric conditions. Aggregation of ice crystals is not included in the scheme. For low temperature ( $T < 235$  K) it is assumed that this process is quite negligible (Kajikawa and Heymsfield, 1989).

### 3. Case study

A real meteorological case with a potentially unstable layer in the tropopause region is presented here. For this purpose we use high resolution radiosonde data

(Spichtinger et al., 2003a) and meteorological analyses from the European Centre for Medium-Range Weather Forecasts (ECMWF). Ice supersaturation in the upper troposphere was measured in a routine radiosonde ascent at 06 UTC on 16 September 2000, over the Richard-Assmann-Observatory, Lindenberg, Germany.

#### 3.1. Meteorological situation and measurements

The meteorological situation over Central Europe is dominated by a small low pressure system (central pressure minimum  $p \sim 1001$  hPa over the Netherlands at 00UTC). Actually, a weak warm front extends from southern Denmark to about Czech Republic (see Fig. 1). Lagrangian trajectory are calculated for investigations of large-scale motions in the upper troposphere. We use the Lagrangian Analysis Tool (LAGRANTO, see Wernli and Davies, 1997) driven by wind fields of the operational meteorological analyses obtained from ECMWF. The data are available on a horizontal Gaussian grid with increments of  $0.25^\circ$ , and 60 vertical levels with a typical vertical resolution of about  $\Delta p \sim 30$  hPa in the upper troposphere. The ‘starting’ region for backward trajectory calculations is an upper tropospheric region centred around Lindenberg (coordinates:  $14.12^\circ\text{E}/52.20^\circ\text{N}$ ):  $13 \leq \text{longitude} \leq 15^\circ\text{E}$ ,  $51.5 \leq \text{latitude} \leq 52.5^\circ\text{N}$ ,  $225 \leq p \leq 350$  hPa.

The flow is represented by the time evolution of air parcels along the trajectories as given in Fig. 2 (vertical coordinate is pressure). The time interval for the backward calculations is 42 h. The large-scale flow is driven by the small low pressure system. At least during the last 12 h before the trajectories reach target region around

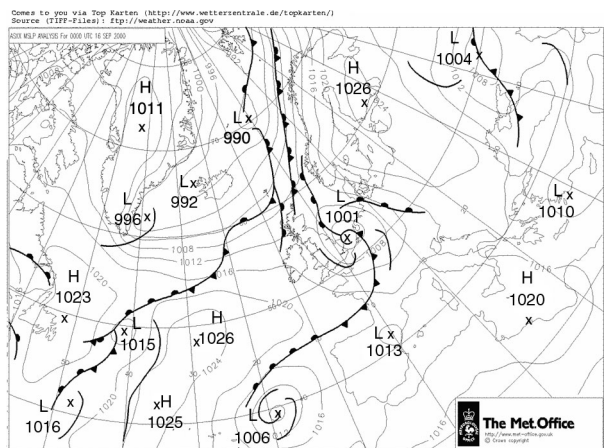


Fig. 1. Meteorological situation at 00 UTC, 16 September 2000 from Bracknell UK MetOffice Analysis for surface pressure including fronts. This analysis was kindly provided by UK Met Office under open Government Licence (see also <http://www.nationalarchives.gov.uk/doc/open-government-licence/>).

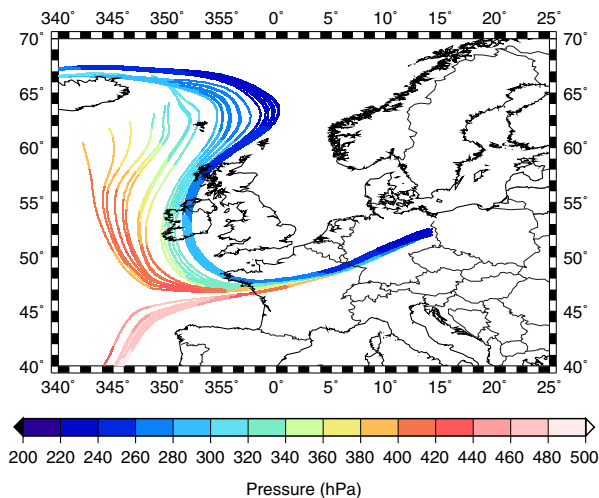


Fig. 2. Backward trajectory calculations with LAGRANTO (for 42 h). The colour indicate altitude in pressure coordinates. Note, that the air masses are quite collocated in the vertical direction after passing about longitude  $\lambda \approx 0^\circ$ , which corresponds roughly to a time of  $t = 12\text{--}14$  h relative to the starting point. The upward motion during the last 6 h correspond to a median value of  $\text{med}(w) \sim 0.03 \text{ m s}^{-1}$ .

Lindenberg the flow direction on different vertical model levels is almost identical; thus, the set of trajectories represents more a layer than single parcels. This can be seen clearly in the time evolution of temperature and pressure along the trajectories (Fig. 3). Indeed, the whole layer is lifted moderately during this time from  $250 \leq p \leq 400$  hPa at  $-12$  h ( $\equiv 15$  September 2000, 18 UTC) to  $225 \leq p \leq 325$  hPa at 0 h ( $\equiv 16$  September 2000, 06 UTC); the upward motion is quite homogeneous and can be estimated within the range  $0.00 \leq w \leq 0.06 \text{ m s}^{-1}$  with a median of about  $\text{med}(w) \sim 0.03 \text{ m s}^{-1}$ .

From a routine radiosonde ascent at 06 UTC, started at Richard-Assmann-Observatory Lindenberg we obtain corrected humidity data (Spichtinger et al., 2003a; Leiterer et al., 2005). Additionally, we use a ‘pseudo radiosonde’ ascent, that is, a vertical column from ECMWF analysis for the grid point nearest to the radiosonde’s position in the upper troposphere. The drift of the radiosonde in altitudes  $8 \leq z \leq 12$  km is in the range 10–21.5 km because of weak horizontal winds; therefore the grid point  $14.25^\circ\text{E}/52.25^\circ\text{N}$  is chosen for the pseudo radio soundings. In Fig. 4, vertical profiles of temperature, relative humidity over ice, potential temperature and horizontal wind speed, respectively, are shown. In the upper troposphere ( $9000 \leq z \leq 11,000$  m) high ice supersaturation could be found in the radiosonde data. Even the corrected radiosonde cannot represent values of  $RHi > 140\%$ ; thus, a dry bias is still possible (Leiterer et al., 2005). ECMWF analyses also indicate slight ice supersaturation in this altitude range, but the vertical

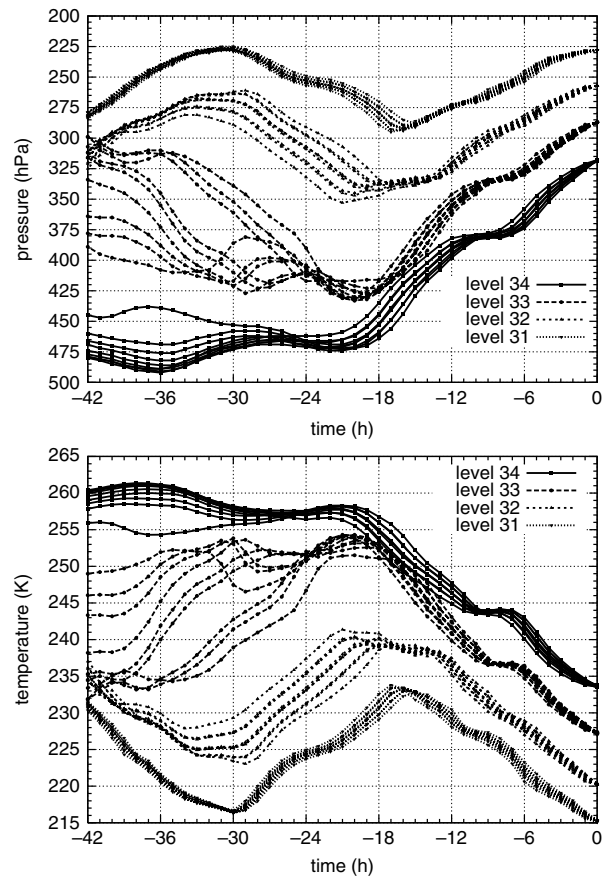


Fig. 3. Backward trajectory calculations for investigating the air streams, started at  $t = 0$  h (corresponding to 06 UTC, 16 September 2000) at ECMWF model levels 31–34. On the top panel, the altitude in pressure coordinates is shown, whereas on the bottom panel the temperature evolution is displayed.

structure is not well captured. The temperature profiles agree quite well (Fig. 4, left panel).

We investigate the thermal stability inside the super-saturated layer. The potential temperature profile is weakly stable (Brunt–Vaisala frequency  $N < 0.007 \text{ s}^{-1}$ ) with two embedded thin unstable layers ( $N^2 \sim -5 \cdot 10^{-5} \text{ s}^{-2}$ ). For including the effect of water vapour and ice, we use an adapted version of equivalent potential temperature for phase transitions ice–vapour, which is (nearly) conserved for adiabatic processes including phase changes in the low temperature regime ( $T < 235$  K):

$$\theta_e = T \left( \frac{p_0}{p} \right)^{\frac{\kappa}{c_p}} \cdot \exp \left( \frac{L_s q}{c_p T} \right) \quad (4)$$

For investigating potential instabilities, we adopt the classical definition from cloud dynamics as given for

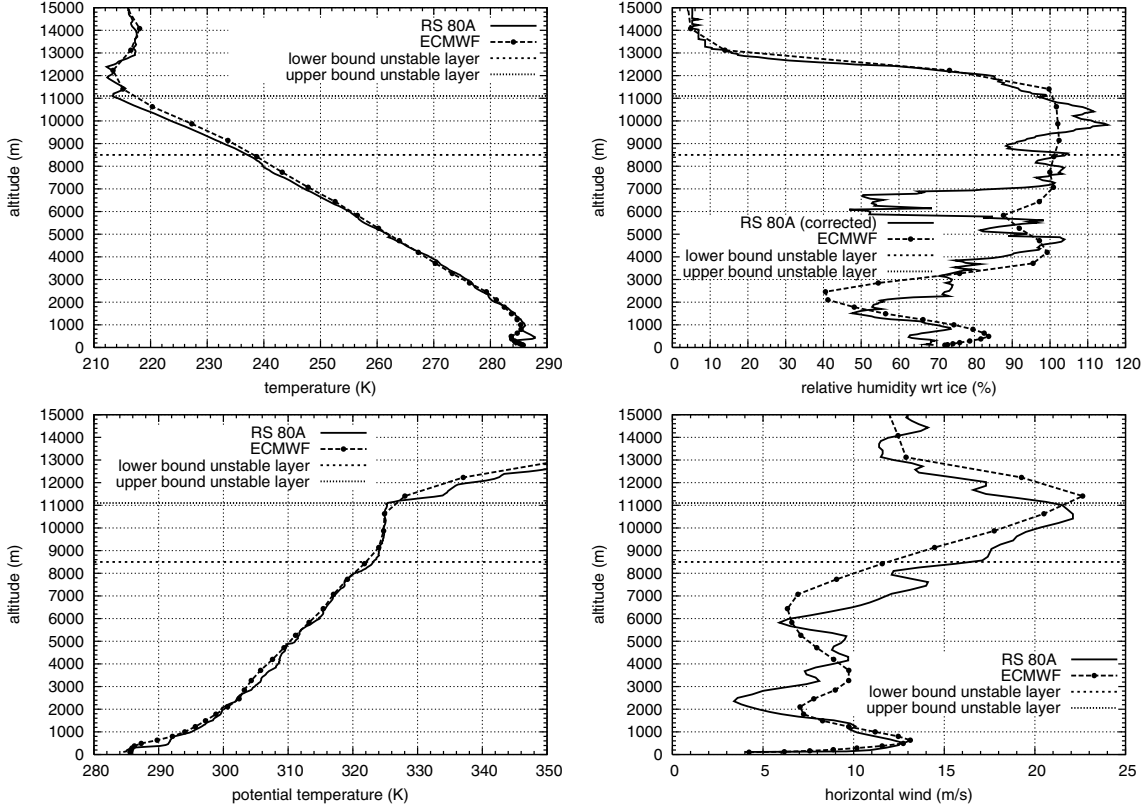


Fig. 4. Vertical profiles of temperature, relative humidity over ice, potential temperature and horizontal wind, respectively, from high-resolution radiosonde data ( $\Delta z \sim 50$  m) and ECMWF operational analyses are shown. Additionally, the upper and lower boundary of the potentially unstable layer are indicated in the profiles, as derived from equivalent potential temperature.

the standard equivalent potential temperature (e.g. Lin, 2008):

$$\frac{\partial \theta_e}{\partial z} \begin{cases} > 0 & \Leftrightarrow \text{potentially stable} \\ = 0 & \Leftrightarrow \text{potentially neutral} \\ < 0 & \Leftrightarrow \text{potentially unstable} \end{cases} \quad (5)$$

Potential stability characterises stability for lifting of whole layers in contrast to static and conditional stability, which always refers to a single parcel. Our trajectory

calculations indicate a layer lifting; thus, the use of equivalent potential temperature gradient as indication of potential instability is justified. A potentially neutral or even slightly unstable layer is found in the altitude range  $8500 \leq z \leq 11,100$  m (Fig. 5, right panel), almost coincident with the ice-supersaturated layer. The potentially unstable layer can also be estimated from the ascent velocity  $dz/dt$  of the radiosonde. The mean vertical velocity averaged over the whole ascent is about  $\langle dz/dt \rangle \approx 5.15 \text{ m s}^{-1}$ . The deviation

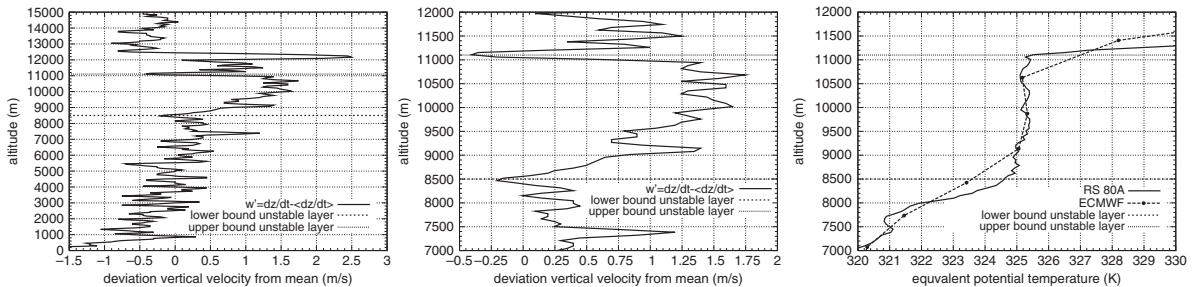


Fig. 5. Determination of unstable layer using 'vertical velocity' as derived from radiosonde data and equivalent potential temperature. On the left panel the vertical velocity perturbation relative to the mean value for radiosonde ascent ( $\langle w \rangle = 5.15 \text{ m s}^{-1}$ ) is shown. The middle panel represents a zoom of the left panel into the interesting altitude range of  $7 \leq z \leq 12$  km. For comparison, the equivalent potential temperature profiles (radiosonde/ECMWF) are shown in the right panel.



from the mean value is given by  $w' = dz/dt - \langle dz/dt \rangle$ .  $w'$  shows considerably higher values in the altitude range  $8500 \leq z \leq 11,100$  m with very pronounced minima at the boundaries (Fig. 5). Thus, both potential temperature and the ‘derived’ vertical velocity show the existence of an unstable layer. ECMWF data also represent the potentially unstable layer, although its vertical extension is smaller (altitude range  $\sim 9500 \leq z \leq 10,600$  m), probably due to coarse data resolution. Ice water content values  $IWC > 0$  from ECMWF analysis data indicate a cirrus cloud in the altitude range of the ice-supersaturated layer. From satellite images (see Fig. 6) the occurrence of a thick cirrus cloud over Central Europe can be confirmed.

In summary, there are some indications for a (thick) cirrus cloud and ice supersaturation within a potentially unstable layer. In the next section, the formation and evolution of a cirrus cloud under these special conditions will be investigated using the cirrus cloud model as described in Section 2.

### 3.2. Setup for simulations

We run model simulations for interpretation of measurements and analysis data in the following setup. We use a 2D domain ( $x$ - $z$ -plane) in the middle and upper troposphere with a horizontal extension of  $L_x = 51.1$  km (horizontal resolution  $\Delta x = 100$  m) and a vertical altitude range of  $4 \leq z \leq 14$  km (vertical resolution  $\Delta z = 50$  m). The total

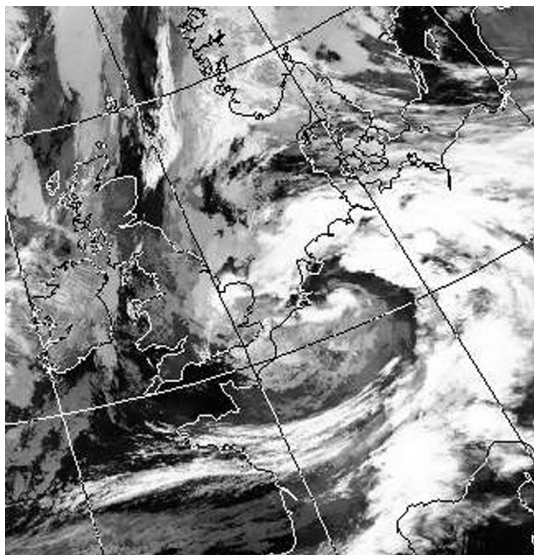


Fig. 6. AVHRR image (channel 5:  $\lambda = 11.5\text{--}12.5\mu\text{ m}$ ) at 05:31 UTC, September 16, 2000, showing thick cirrus clouds over Germany. This satellite image was kindly provided by NERC Satellite Receiving Station, Dundee University, Scotland (<http://www.sat.dundee.ac.uk/>).

simulation time is set to  $t_{tot} = 400$  min with a dynamical time step of  $\Delta t = 1$  s and an optional microphysical time step of  $\Delta t_{mp} = 0.1$  s (in case of homogeneous nucleation and/or fast ice crystal growth, see Spichtinger and Gierens, 2009a, for details). The output data is written with a time increment of 5 min. The whole 2D domain is constantly lifted by a constant large-scale updraught of  $w_{LS} = 0.03$  m s<sup>-1</sup> consistent with trajectory calculations. Figures 7 and 8 show the initial vertical profiles for the model. They are chosen to match the real profiles as good as possible after some simulation time. Thus, the initial profiles do not necessarily represent the observations at 16 September 2000, 06 UTC. In order to obtain a better agreement with the measurements in course of the simulation, the initial profiles were shifted downwards by  $\Delta z = 360$  m, such that they match the measurements at  $t \sim 190\text{--}210$  min.

An ice-supersaturated layer is prescribed in the altitude range  $8.4 \leq z \leq 9.55$  km. While the (dry) potential temperature indicates stable stratification for the upper troposphere, the addition of moisture in the ice-supersaturated layer leads to a potentially unstable layer in the altitude range  $8.5 \leq z \leq 10$  km. The potential temperature field is superimposed by a Gaussian noise with a standard deviation of  $\sigma_\theta = 0.05$  K. These initial perturbations lead in turn to initial variations in vertical velocity. As described in the next section, these initial perturbations organise themselves and remain persistent with slightly decreasing amplitude due to dissipation.

### 3.3. Results

We investigate the convective cell formation and evolution, the microphysical and dynamical properties of the cells and the humidity fields inside the cells. This leads us to the main issue, namely high supersaturation inside thick cirrus clouds. As stated in the introduction, clear definitions on ‘high supersaturation’ and ‘thick clouds’ are usually missing in the discussion of ice supersaturation inside cirrus. For our analysis, we will use the following, more precise definitions:

**High supersaturation** is equivalent to values  $S_i \geq 12$ , **very high supersaturation** is equivalent to values  $S_i \geq 1.4$ . This definition is motivated by typical thresholds for ice nucleation (Koop et al., 2000; DeMott et al., 2003). For cloudy data points we will use the following definitions:

**Thick cirrus cloud** is equivalent to values of ice water content  $IWC \geq 10$  mg m<sup>-3</sup>, **very thick cirrus cloud** is equivalent to values of ice water content  $IWC \geq 30$  mg m<sup>-3</sup>. These values are estimated using mean temperature  $\bar{T} \sim 230$  K and pressure  $\bar{p} \sim 300$  hPa, respectively, for the corresponding saturation mixing ratio  $q_s(p, T) = e^{\frac{v_i(T)}{p}}$ . This quantity can be seen as reservoir for clouds, as in

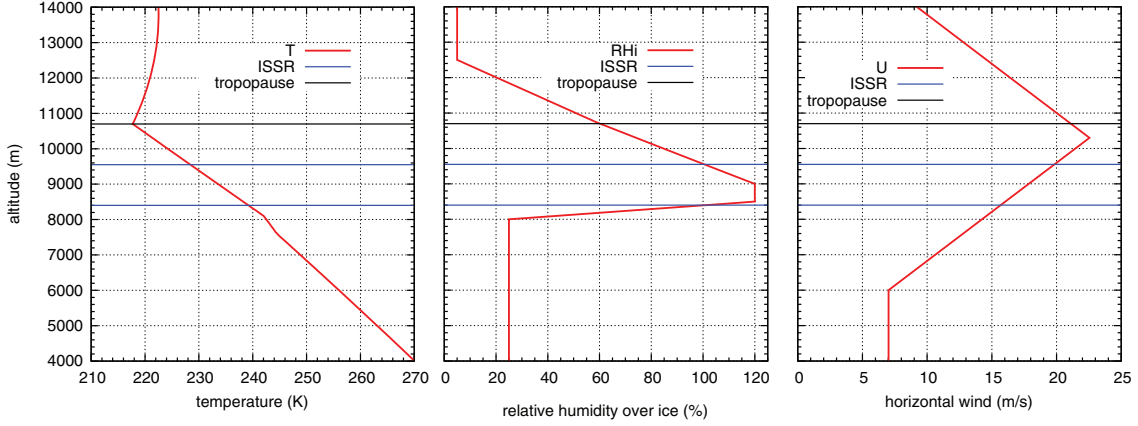


Fig. 7. Initial profiles of temperature, relative humidity over ice and horizontal wind, respectively, for realistic simulations with the EULAG model.

former studies (e.g. Klein and Majda, 2006), that is, we set  $q_c = f \cdot q_s$  with  $f \sim 0.1$  or  $f \sim 0.33$  for thick or very thick cirrus clouds, respectively.

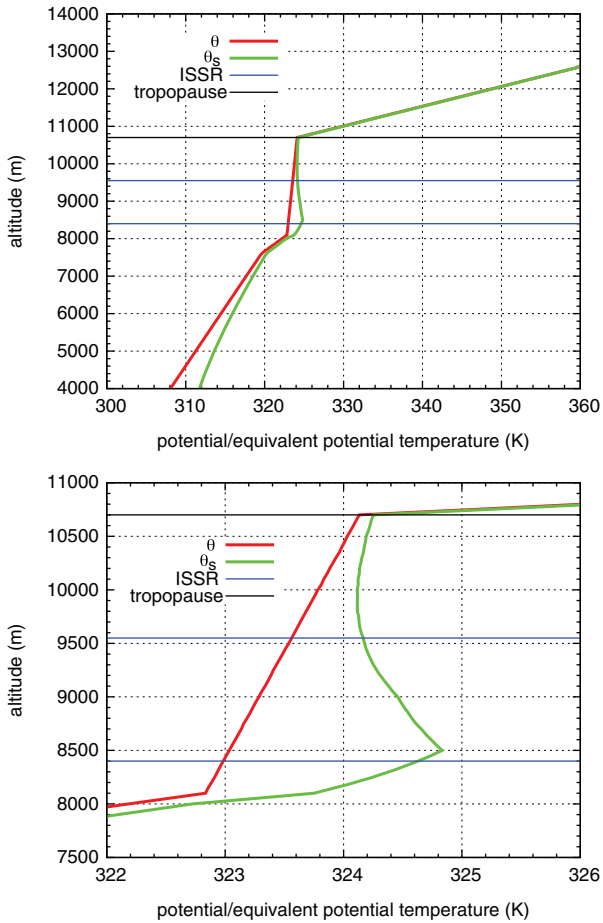


Fig. 8. Initial profiles of potential and equivalent potential temperature for realistic simulations with the EULAG model. Top: Whole vertical profile, bottom: Zoom into potentially unstable layer.

3.3.1. *2D structure of the formed cirrus clouds.* Figures 9 and 10 show the time evolution of cloud formation and development of convective cells. The entire 2D domain is lifted by a constant updraught of  $w_{LS} = 0.03 \text{ m s}^{-1}$  and relative humidity over ice increases in reaction on this large-scale motion. The initially perturbed potential temperature field organise to larger structures under the influence of the moderate wind shear ( $\partial u / \partial z = 3.6 \cdot 10^{-1} \text{ s}^{-1}$ ). Small eddies form, leading to structured upward and downward motions. This organisation of an originally randomly disturbed temperature field into larger structures was already seen for simulations in a more stable environment (Spichtinger and Gierens, 2009b). The detailed formation mechanism of these structures remains unclear; wind shear might play a major role by generating vorticity in the  $x$ - $z$ -plane. The eddies have a horizontal extension of few km and a vertical extension of  $\sim 0.5$ – $1 \text{ km}$  as estimated from the turbulent kinetic energy field (not shown). The induced vertical velocity is quite small ( $-0.08 \leq w' \leq 0.08 \text{ m s}^{-1}$ , with  $w' = w - w_{LS}$ ) in the initial phase ( $t \leq 80 \text{ min}$ ). The additional temperature changes driven by small-scale eddies lead to an increase in relative humidity over ice and to a fairly inhomogeneous but structured 2D distribution of  $RH_i$ . In some small regions the thresholds for homogeneous nucleation are surpassed; ice crystals are formed in the lower part of the ice-supersaturated layer at around  $t \sim 55 \text{ min}$  and later. Because ice formation is triggered first in the lower part of the ice-supersaturated region ( $8.5 \leq z \leq 9 \text{ km}$ ) at quite high temperatures ( $230 \leq T \leq 236 \text{ K}$ ), only few ice crystals are formed in these regions ( $N_i \sim 10 \text{ L}^{-1}$ ). Although these ice crystals can grow without competition in a highly supersaturated environment, it takes some time until considerable latent heat is released. The addition of latent heat contributes to a further enhancement of the existing eddies; cells containing ice crystals are formed. At  $t \sim 105 \text{ min}$



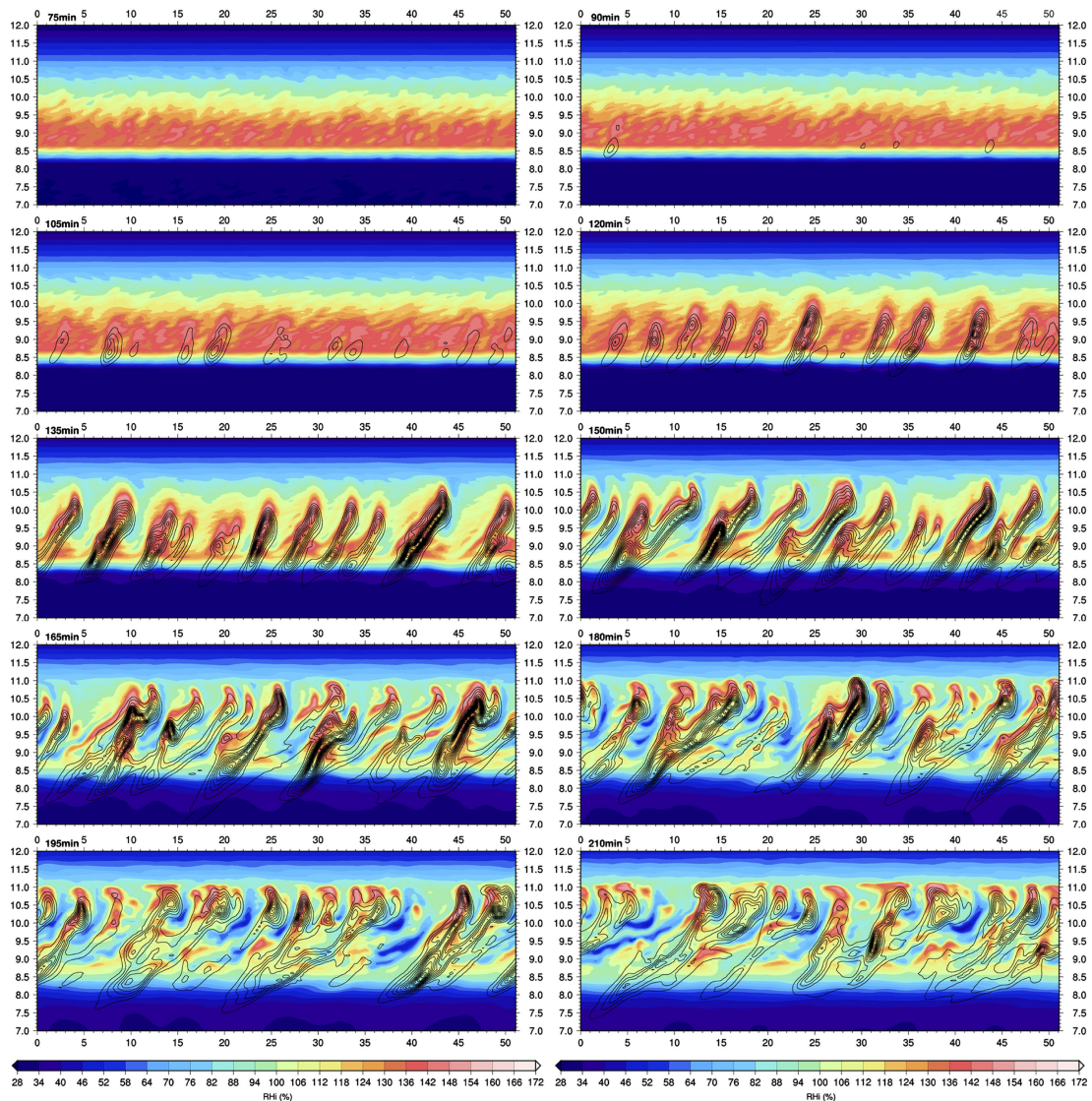


Fig. 9. Time evolution of convective cells inside the ISSR in the  $x$ - $z$ -plane (horizontal extension in kilometres vs. altitude in kilometres) – early stage of cirrus cloud ( $t = 75, 90, 105, 120, 135, 150, 165, 180, 195, 210$  min). Colour bar: relative humidity over ice, black lines: isolines of ice water content (increment:  $\Delta\text{IWC} = 5 \text{ mg m}^{-3}$ ).

(see Fig. 9) more than 10 convective cells can be seen, visualised by their ice water content (black isolines). In the following, the cells grow in vertical direction due to latent heat release, reaching higher levels of the ice-supersaturated layer. Horizontal wind shear has an impact on the shape of the developing cells. In the lower part of the domain (i.e.  $8 \leq z \leq 10$  km), the wind is increasing with height, tilting convective cells to the right. As soon as the cells reach levels around  $z \sim 10$  km (maximum wind, change of wind shear), they tend to rise almost directly upwards. After reaching the negatively sheared region above wind maximum the cells are pushed to the left, inducing overturning of the cells. The rising convective cells are stopped

at the tropopause. The buoyancy of the cells is not sufficient that they can penetrate into the highly stratified stratosphere. Since the vertical extension of the layer with convective activity is quite shallow, we call the phenomenon **shallow cirrus convection** in analogy to shallow convection in liquid clouds. The main convective activity takes place in the time interval  $120 \leq t \leq 240$  min. However, also at later stage of the simulations few convective cells are triggered, leading to some inhomogeneities in a quite mixed layer cloud. We will see later that the convective activity is not strong enough to produce a well-mixed layer, thus potentially unstable regions can exist over the whole simulation time.

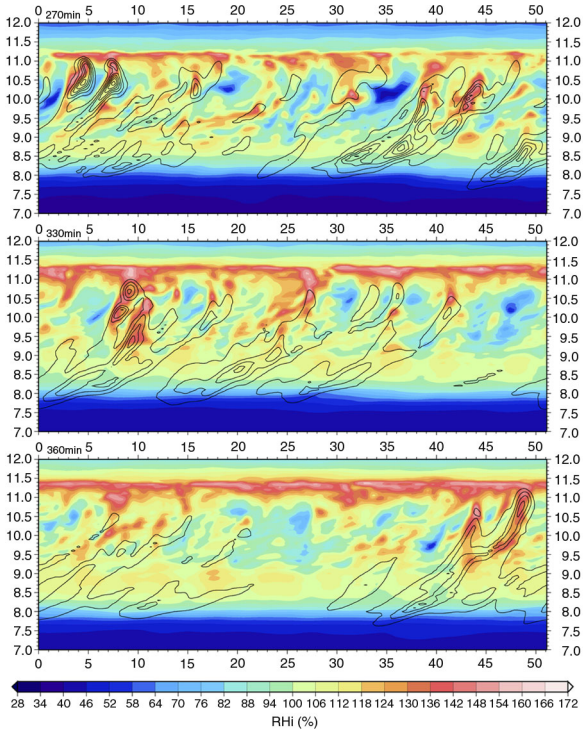


Fig. 10. Time evolution of convective cells and the layer cloud in the  $x$ - $z$ -plane (horizontal extension in kilometres vs. altitude in kilometres) at a later stage ( $t = 270/330/360$  min). Colour bar: relative humidity over ice, black lines: isolines of ice water content (increment:  $\Delta IWC = 5 \text{ mg m}^{-3}$ ).

The cloud structure of the formed cloud is determined by the general behaviour of the convective cells. Ice crystals inside the cells are lifted by cell's updraught until they grow to large sizes such that their terminal velocities are larger than vertical updraughts. Sedimenting ice crystals form the typical fall streaks, reaching from the top of the convective cells over the whole range of the supersaturated layer far down into the subsaturated layer below.

**3.3.2. Dynamical vs. microphysical aspects of convective cells.** The dynamic mechanism of cell formation and evolution for shallow cirrus convection is almost identical to classical cloud dynamics of liquid clouds. The existing condensate (water or ice) acts as sink for supersaturated water vapour. The vapour condenses on the stable phase (liquid or solid) and latent heat is released. Thus, in a potentially unstable environment the temperature inside cloud elements is higher than in the cloud free environment. This difference produces an intrinsic updraught region inside the cloud. The changed velocity field leads also to a cell formation, that is, structures larger than the initial cloud element are formed.

In contrast to condensation of liquid cloud droplets, ice formation requires high supersaturations (Koop et al., 2000; DeMott et al., 2003); this leads to some special features in the cell formation and evolution. We discuss some aspects of the evolution of a single cell in more details in the following. For determining the dominant processes, we also investigate timescales for (a) changing relative humidity and (b) changing ice mass concentration  $q_c$ , that is,

$$\frac{dRH_i}{dt} = \frac{RH_i}{\tau_{cool}} + \frac{RH_i}{\tau_{phase}} + \frac{RH_i}{\tau_{mix,RH_i}} \quad (6)$$

$$\frac{dq_c}{dt} = \frac{q_c}{\tau_{growth}} + \frac{q_c}{\tau_{sed}} + \frac{q_c}{\tau_{mix,q_c}} \quad (7)$$

The timescales are defined in the Appendix. For the analysis of the different processes we use ratios of the absolute values of timescales  $r = \left| \frac{\tau_1}{\tau_2} \right|$ . The interpretation is quite straightforward. A timescale ratio  $r > 1 \Leftrightarrow |\tau_1| > |\tau_2|$  indicate a dominant process  $r \approx 1 \Leftrightarrow |\tau_1| \approx |\tau_2|$  indicates that both processes are of comparable strength; finally, for  $r < 1 \Leftrightarrow |\tau_1| < |\tau_2|$  process 1 is dominant. This type of analysis is also represented in Figs. 12 and 13.

There are different stages of a typical cell in ice-supersaturated air, summarised as follows:

- The large-scale updraughts in combination with small-scale eddies induce first nucleation events. Since the nucleation takes place at (1) low vertical velocities ( $w \leq 0.02\text{--}0.05 \text{ m s}^{-1}$ ) and (2) high temperatures (i.e. at the lower boundary of the supersaturated layer), just few ice crystals are produced ( $N_i \sim 10\text{--}20 \text{ L}^{-1}$ ). These crystals can grow to large sizes in the highly supersaturated environment and in the further evolution they sediment. Because of small surface area of ice crystals, the consumption of water vapour is quite ineffective; the latent heat release leads to small additional values of vertical velocity. Secondary nucleation events follows in the enhanced vertical velocity, leading to higher ice crystal number concentrations. Falling ice particles form the first fall streaks, removing ice mass from the nucleation zone.
- The cell starts to organise due to changes in the velocity field; a confined updraught region is formed with vertical velocity increasing in time. The ice crystals inside the cell grow further, consuming ice supersaturation. On the other hand, rising of the cells and thus adiabatic cooling leads to a source of ice supersaturation. Timescale analysis (see below) shows that cooling is almost always dominant over

growth and/or mixing. High supersaturation values are found inside the cells.

- Sedimentation forms fall streaks, extending from the top of the cells down to the lower boundary of the supersaturated layer and far beyond into subsaturated air. This is a very clear macroscopic signature of the convective cells.
- The cell rises until level of neutral buoyancy is reached. The cell is then overturning and sinks downwards; it disappears and the ice crystals sediment and evaporate in the subsaturated air.

An example of single cell evolution in its developing stage is shown in Fig. 11. Here, the cell is tracked and displayed with a time increment of  $\Delta t = 10$  min; the variables potential temperature perturbation, vertical velocity, relative humidity over ice, ice crystal mass and number concentration, respectively, are shown. On the left panels, the 2D structure of the cell is shown; on the right panel, vertical profiles as given at the centre of the cell are shown. Two important features can be seen:

- (1) Inside the cells no further ice nucleation takes place ('quenching' of nucleation), that is, at the maximum updraught values, diffusional growth is always large enough to keep supersaturation values below homogeneous freezing thresholds. On top of the cells, nucleation events are triggered, that is, at lower vertical velocities.
- (2) The updraughts triggered by latent heat release also change the velocity fields. Inside the cell upward motion can be found, whereas laterally downdraughts are induced. Thus, relative humidity is reduced in the ambient air due to adiabatic compression in the downdraughts. Again, the 'cooling' timescale is smaller than the 'growth' timescale. This means that relative humidity is faster reduced by warming than it is enhanced by sublimating ice crystals.

High supersaturation inside cells is triggered by dominance of cooling as source for supersaturation and the ability of ice crystals inside the cells to reduce the ice supersaturation below homogeneous ice nucleation thresholds. Thus, vertical velocity provides high supersaturation but growth prevents ice nucleation leading to ice supersaturation on high levels. In principle, this feature is similar to modification or even suppression of homogeneous nucleation by few heterogeneously formed and pre-existing ice crystals; also in this case high ice supersaturations can be observed (see, e.g., Gierens, 2003; Ren and MacKenzie, 2005; Spichtinger and Gierens, 2009c; Spichtinger and Cziczko, 2010).

We analyse this behaviour using timescale analysis. In Fig. 12, timescales for cooling, growth and mixing

as well as ratios of timescales are represented at the end of time series in Fig. 11; the cell is in its mature state (simulation time  $t = 130$  min). For processes cooling (or equivalently warming) vs. depositional growth (or equivalently sublimation) the timescale analysis is quite clear. The first term in eq. (3) (driven by vertical velocity) is almost always dominant over the growth/sublimation term, even in different velocity regimes ( $w < 0$  and  $w > 0$ ). It seems that just for values of cloud ice mixing ratio  $q_c > 10^{-5}$  kg/kg, diffusional growth could be of same order than cooling. This dominance can be also seen for the whole simulation data, as represented in the 2D probability distribution of  $\left| \frac{\tau_{phase}}{\tau_{cool}} \right|$  (Fig. 13, upper left panel). For the comparison cooling vs. mixing, we find the same qualitative behaviour. The cooling term is almost always dominating over mixing. This feature can also be seen for the whole simulation in the 2D distribution (Fig. 13, upper right panel) Thus, in the updraughts of the convective cells, ice supersaturation is almost always increased by cooling, whereas neither depositional growth nor mixing is able to reduce ice supersaturation efficiently. The same is true for the downdraught regions. The decrease of relative humidity by warming due to downdraughts is dominating over enhancement of  $RHi$  by sublimating ice crystals or mixed air.

The comparison of timescales for ice mass mixing ratio  $q_c$  shows a different behaviour. Growth and sedimentation are usually of the same order of magnitude. However, large variations can occur; both scenarios are possible, that is,  $|\tau_{dep}| < |\tau_{sed}|$  and  $|\tau_{dep}| > |\tau_{sed}|$ . This behaviour can be seen in the snapshots at simulation time  $t = 130$  min (Fig. 12) as well as in the overall picture (2D distribution in Fig. 13, lower left panel). The comparison between sedimentation and mixing shows a slightly different behaviour. Sedimentation is almost always dominating over mixing ( $|\tau_{sed}| < |\tau_{mix,q_c}|$ ), that is, changes by sedimenting ice crystals are usually much faster than changes due to mixing of air due to local dynamics. This behaviour can be seen for the cell at simulation time  $t = 130$  min (Fig. 12) as well as in the 2D probability distribution (Fig. 13, lower right panel).

For the time evolution of tracked cells, a typical life time of the cells, from first nucleation events to the decaying of the cell, can be estimated:  $t_{life} \sim 90$  min. The ice supersaturation inside the cell is just present as long as the intrinsic updraught is maintained by the latent heat release.

### 3.3.3. Statistics of relative humidity inside cirrus clouds.

In detailed investigation of cloud evolution, single cells and timescales, we have seen that ice supersaturation inside convective cells is possible and quite frequent. From snapshots in Fig. 11 it is not possible to estimate



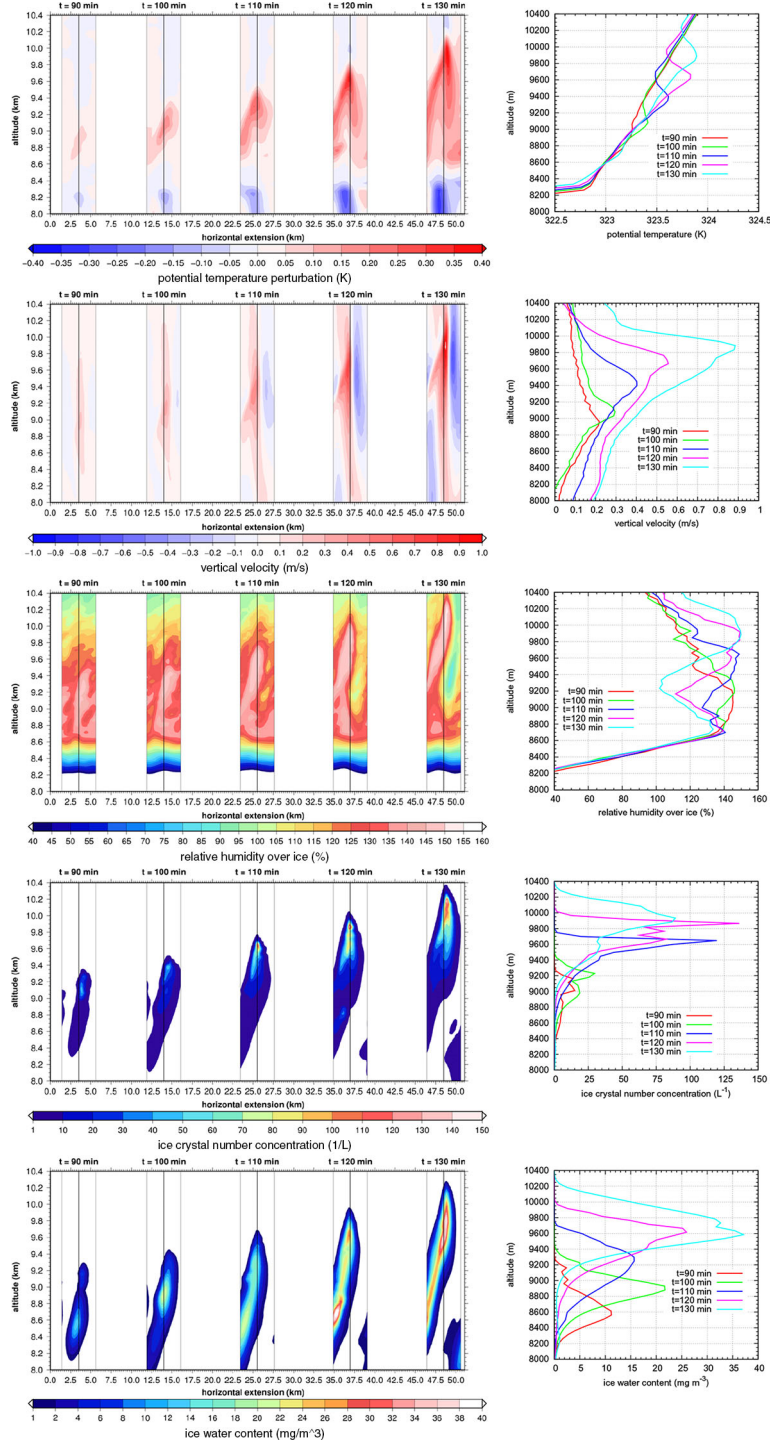


*Fig. 11.* Time evolution of a tracked cell during the time interval  $90 \leq t \leq 130$  min ( $\Delta t = 10$  min). The panel shows the time evolution of vertical velocity perturbations, relative humidity over ice, ice crystal number concentrations and ice water content, respectively. Left: 2D structure of the cell. Right: Vertical profiles at the centre of the cell.

the frequency of occurrence of such events. Therefore, we present a two-dimensional probability density for relative humidity and ice water content in Fig. 14. All data from the whole simulation are used; the criterion of ‘cloudy data’

was determined by a threshold of ice number concentration. A data point is marked as **cloudy** if the ice crystal number concentration exceeds the value  $N_{i,thers} = 1 \text{ L}^{-1}$ . This threshold corresponds quite well to the typical

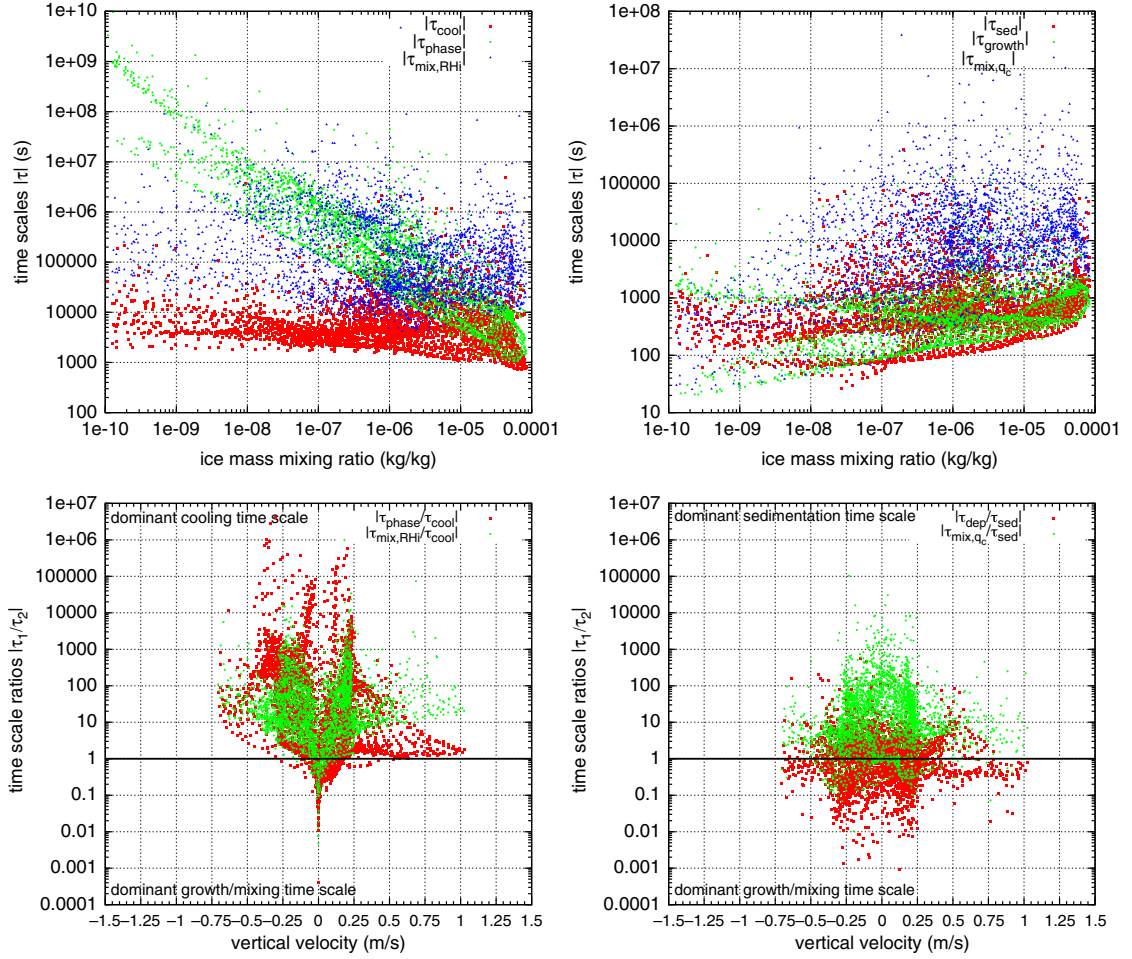


Fig. 12. Timescales and timescale ratios for the tracked cell at simulation time  $t = 130$  min. Top row: Timescales vs. ice mass mixing ratio for relative humidity timescales (left panel) and ice mass concentration timescales (right panel). Bottom row: Timescale ratios vs. vertical velocity for relative humidity timescales (left panel) and ice mass concentration timescales (right panel).

detection limit for in situ measurements (see, e.g., Krämer et al., 2009). Primarily, we are interested in ice supersaturation inside clouds. For consistency, we present the 2D distribution for the relative humidity range  $30\% \leq RH_i \leq 160\%$  and the ice water content interval  $0 \leq IWC \leq 90 \text{ mg m}^{-3}$ . The probability distribution is quite broad with a maximum around  $(RH_i, IWC) \approx (105\%, 5 \text{ mg m}^{-3})$ . This enhanced relative humidity over ice is consistent with a permanent supersaturation source by large-scale dynamics  $w_{LS} = 0.03 \text{ m s}^{-1}$ . Several additional features can be seen (all values of frequency of occurrence are represented in Table 1):

- Ice clouds are usually not in thermodynamic equilibrium, only about 11.5% of all cloud events are close to saturation ( $RH_i \sim 100\%$ , i.e.,  $98.5\% \leq RH_i \leq 102.5\%$ ). The relative humidity inside clouds range between strong subsaturation ( $RH_i \sim 30\%$ ) and high supersaturation ( $RH_i \sim 160\%$ ). The reason for this

feature is the slow relaxation due to long growth timescales at cold temperatures (in the usual typical range  $10^3 \text{ s} \leq \tau_{\text{phase}} \leq 10^{10} \text{ s}$ , see Fig. 12).

- For shallow cirrus convection, more ice clouds are in the supersaturated stage than in the subsaturated stage. Actually, in 52% of all cloud events ice supersaturation can be found ( $RH_i > 100\%$ ), 36.5% of all cloud cases are present in subsaturated air ( $RH_i < 100\%$ ).
- Ice supersaturation inside thick cirrus clouds ( $IWC \geq 10 \text{ mg m}^{-3}$ ) occurs quite often (about 14% of all cloud events); very high supersaturations up to  $RH_i \sim 150\%$  are possible. The frequency of occurrence for ice supersaturation in very thick clouds ( $IWC \geq 30 \text{ mg m}^{-3}$ ) is still not negligible (about 1.7% of all cloud events)

The two-dimensional probability distribution shows that ice supersaturation inside cirrus clouds is quite common

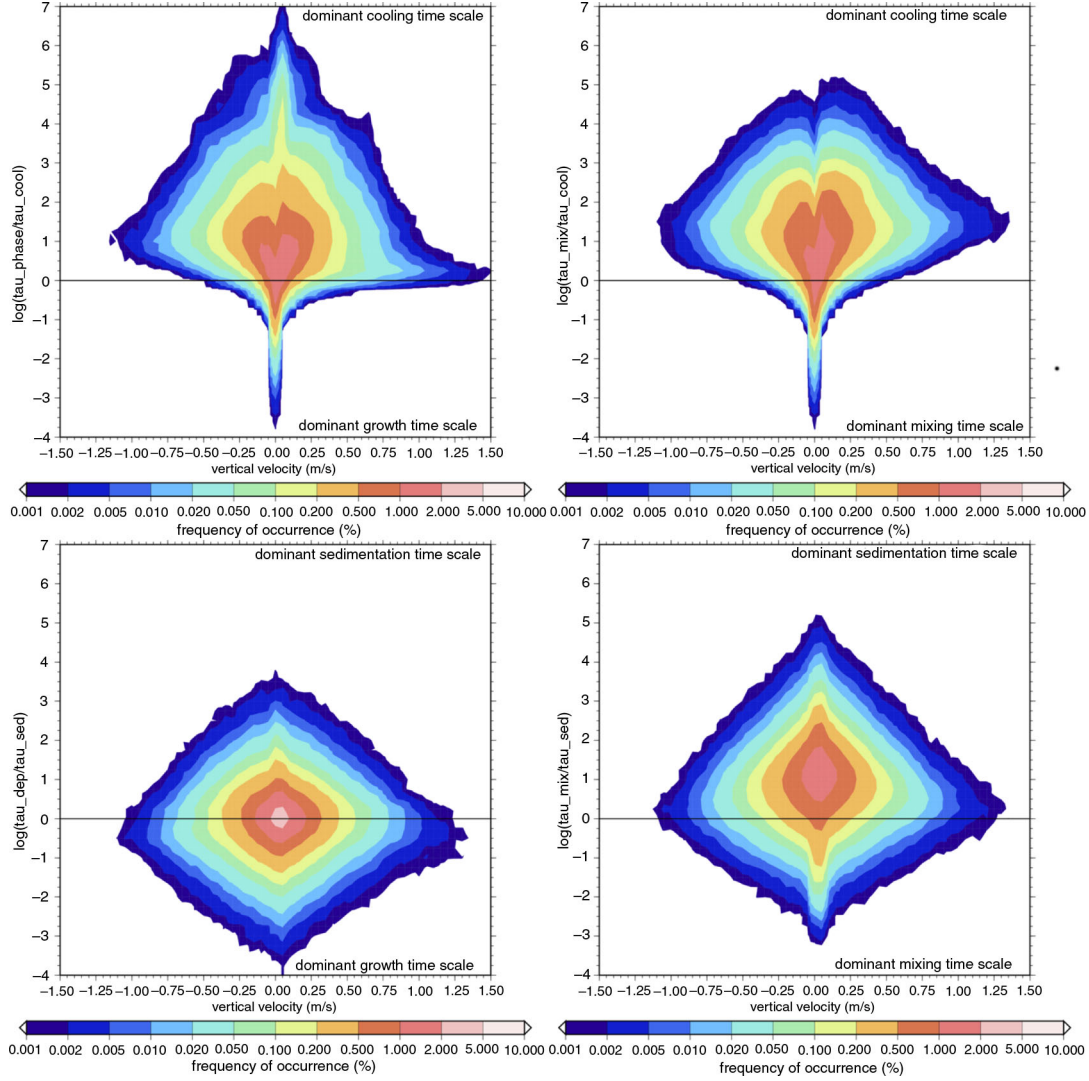


Fig. 13. Timescales for the whole simulation time. Top row:  $RH_i$  timescale ratios, left: ratios  $|\tau_{phase}/\tau_{cool}|$ ; right:  $|\tau_{mix,RH_i}/\tau_{sed}|$ . Bottom row:  $q_c$  timescale ratios, left: ratios  $|\tau_{growth}/\tau_{sed}|$ , right:  $|\tau_{mix,q_c}/\tau_{sed}|$ .

in case of shallow cirrus convection. We note here that the probability distribution does not allow to estimate how long an air parcel inside a cirrus cloud is in the status of ice supersaturation (duration or persistence of supersaturation). The evolution of cells in Fig. 11 shows that ice supersaturation in shallow cirrus convection is a transient phenomenon, triggered by vertical updraughts inside the cells and their lifetime. Generally, we tend to believe that if measurements along flight tracks show many data points in supersaturated air that these measurements represent persistent supersaturation. This is not necessarily true, as shown in the simulated situation.

We additionally show probability distributions of relative humidity over ice for different parts of the simulation. During the time interval  $60 \leq t \leq 210$  min convective

cells are triggered and they dominate the cloud structure. In the later period  $210 \leq t \leq 400$  min the convective activity is reduced. There are still some convective cells, however, the situation is more like a layer cloud, as driven by large-scale motion. Again, we discriminate between clear air and cloudy air by a threshold for ice crystal number concentration  $N_{i,thres} = 1 \text{ L}^{-1}$ .

The probability density of relative humidity over ice shows quite different behaviour for the two time periods (Fig. 15). During the phase of active convection, high relative humidity values are quite frequent inside and outside clouds due to vertical updraughts triggered by the cells themselves. The distribution for relative humidity in clear air is quite ‘flat’, whereas the humidity distribution for cloudy air shows a clear maximum around 105%,



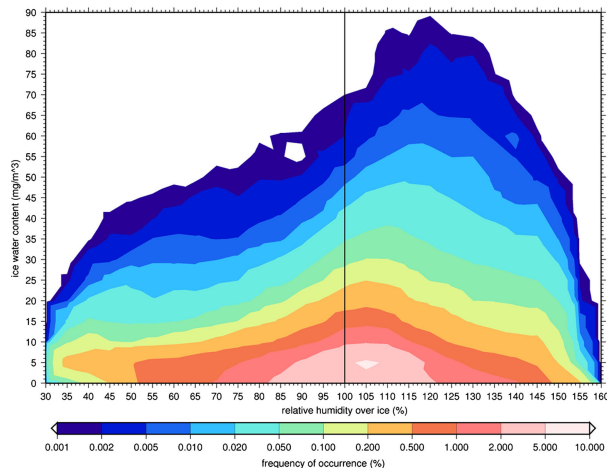


Fig. 14. Joint two-dimensional probability density for relative humidity over ice inside cirrus clouds. The frequency of occurrence for events of certain relative humidity over ice and ice water content is shown for events with ice crystal number concentration larger than  $1\text{ L}^{-1}$ . Thermodynamic equilibrium ( $RHi = 100\%$ ) is indicated by a black line.

as already seen in the 2D distribution in Fig. 14. The distribution has also a clear secondary maximum around 145%. This is direct impact of convective updraughts leading to enhanced supersaturation inside the clouds, as discussed above. In the second time period, we find exponential decay for the supersaturated part of the distributions. In earlier studies this behaviour was already found in observational data obtained by different measurements techniques (Gierens et al., 1999, 2004; Spichtinger et al., 2002, 2003a, 2004; Gettelman et al., 2006). However, it was always assumed (at least implicitly) that this exponential feature would exclusively occur for clear air data, but not for cloudy data. In our investigations the feature is present for both distributions. A simple exponential fit of the form  $p(RHi) = a \cdot \exp(-b \cdot RHi)$  leads to exponents in the range  $0.0425 \leq b \leq 0.073$ , comparable to former studies (Spichtinger et al., 2002, 2003b; Gettelman et al., 2006). It might be that the vigorous dynamics of the convective cells and mixing inside the supersaturated

Table 1. Probability (in percent) for cloudy air ( $N_i \geq 1\text{ L}^{-1}$ ) of a certain state of (super/sub)-saturation and ice water content, respectively

$RHi$	All cloud events	$IWC \geq 10 \frac{\text{mg}}{\text{m}^3}$	$IWC \geq 30 \frac{\text{mg}}{\text{m}^3}$
$RHi \leq 100\%$	36.47	7.36	0.38
$RHi \sim 100\%$	11.49	2.93	0.18
$RHi \geq 100\%$	52.04	14.23	1.68
$RHi \geq 120\%$	20.08	5.68	0.90
$RHi \geq 140\%$	5.24	1.55	0.22

This table represents integrated values of the two-dimensional probability density, as shown in Fig. 14.

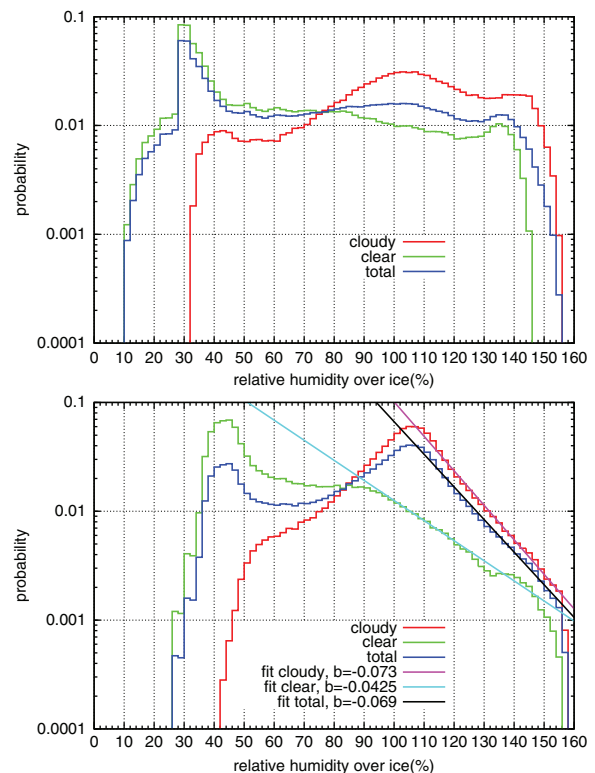


Fig. 15. Probability density of relative humidity over ice in cloudy air (red), clear air (green) and all data (blue) for the time intervals  $60 \leq t \leq 210$  min (top panel, active convection) and  $210 \leq t \leq 400$  min (bottom panel, decaying convection). For the later time period, the distributions are fitted by an exponential distribution of the form  $p(RHi) = a \cdot \exp(-b \cdot RHi)$ . The exponents  $b$  are indicated in the figure.

layer lead to this exponential behaviour, but the exact reason for this feature is still unknown. Beside the exponential behaviour, we see a clear maximum at about  $RHi \sim 105\%$  in the cloudy data, as already shown in the 2D distribution in Fig. 14. As discussed earlier, we would not expect relaxation to saturation since there is a constant source for supersaturation by the large scale updraught  $w_{LS} = 0.03\text{ m s}^{-1}$ .

3.3.4. Statistics of vertical velocity and ice crystal number concentrations. In Fig. 16, we show probability densities of vertical velocity for the two different time intervals as defined above (left panel:  $60 \leq t \leq 210$  min, right panel:  $210 \leq t \leq 400$  min), separated into clear and cloudy air by the ice crystal number concentration threshold  $N_{i,thres} = 1\text{ L}^{-1}$  (see Section 3.3.3). For the first period, the impact of convective cells can be seen quite clearly. The extension to large vertical velocity values is due to the strong upward motions inside the cells and the subsidence around the cells. The structure of the distribution for clear and cloudy

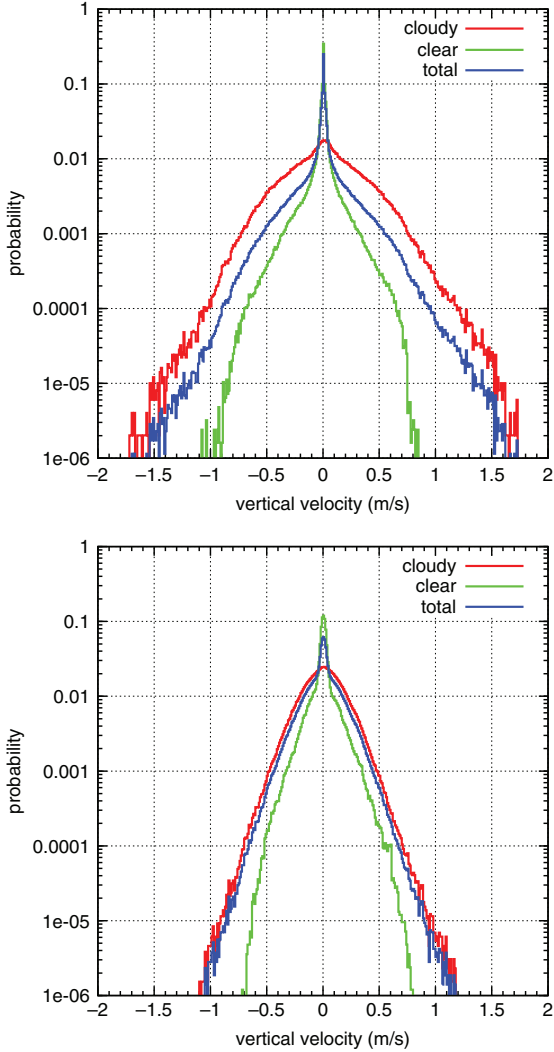


Fig. 16. Probability density of vertical velocity in cloudy air (red), clear air (green) and all data (blue) for the time intervals  $60 \leq t \leq 210$  min (top panel, active convection) and  $210 \leq t \leq 400$  min (bottom panel, decaying convection).

data is quite similar to the ogival shape as reported by Gierens et al. (2007). For clear air data, velocities are systematically lower than for cloudy data; inside clouds, the vertical velocity is triggered by the latent heat release and the maximum updraught is situated **inside** the cell. The rising cell is additionally influencing the air above and around it, leading to enhanced vertical velocities in clear air.

In the second period, the distributions are much more narrow. During this stage, convection is less active than before. Therefore, vertical velocities (inside and outside clouds) are generally smaller. The distribution shows an almost exponential decay in positive and negative velocity range. This behaviour is seen best for cloudy data. Frequency distributions of former measurements also show this

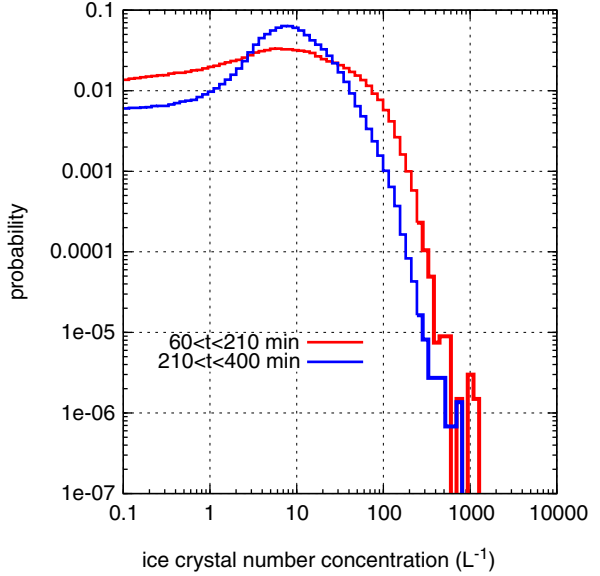


Fig. 17. Probability density of ice crystal number concentrations for the time intervals  $60 \leq t \leq 210$  min (red) and  $210 \leq t \leq 400$  min (blue).

quasi exponential distribution (e.g. during INCA campaign, see Krämer and Ström, 2003).

In Fig. 17, we show probability densities of ice crystal number concentrations for the two different time intervals as defined above (red:  $60 \leq t \leq 210$  min, blue:  $210 \leq t \leq 400$  min). Both distributions peak around  $N_i \sim 5-7 \text{ L}^{-1}$ . The distribution for the first time interval is quite broad. Low ice crystal number concentrations can be produced by weak nucleation events at the very beginning, triggered mainly by the large-scale updraught; the second source for these low concentration is sedimentation of ice crystals leading to a vertical spread and low concentrations (see discussion in Spichtinger and Gierens, 2009b). There is a cut-off for high ice crystal concentrations around  $N_i \sim 1000 \text{ L}^{-1}$ , only three data points show such high concentrations. In the second time interval, the distribution looks very similar, just the maximum is much more pronounced. Low ice crystal number concentrations are consistent with high ice supersaturation values (see discussion in Krämer et al., 2009).

**3.3.5. Mixing of supersaturated layers.** Convection has a strong impact on mixing in the atmosphere. Especially deep convection leads to strong mixing of atmospheric layers; after convection mixed layers show a lapse-rate close to moist adiabatic lapse-rate. In our case of shallow convection inside ice-supersaturated layers, *a priori* it is not clear, which final state will be reached. For a qualitative analysis we investigate mean profiles of (equivalent) potential temperature  $\theta, \theta_e$ . The profiles are averaged over the

horizontal direction. We compare profiles of the vertical layer  $8 \leq z \leq 11$  km from the initialisation of the simulation and at simulation time  $t = 360$  min, when convective activity is very weak. For a better comparison, we shift the vertical profile at  $t = 360$  m downwards by  $\Delta z = 648$  m, such that both profiles are normalised by altitude. From equivalent potential temperature a ‘moist’ Brunt-Vaisala frequency ( $N_m$ ) can be derived, similarly to standard Brunt-Vaisala frequency ( $N$ ):

$$N^2 := \frac{g}{\theta} \frac{\partial \theta}{\partial z}, N_m^2 := \frac{g}{\theta_e} \frac{\partial \theta_e}{\partial z} \quad (8)$$

Figure 18 show vertical profiles of  $\theta, \theta_e$  (upper row) and  $N, N_m$  (lower row) at initialisation (solid line) and at simulation time  $t = 360$  min (dashed line). At the initialisation, the stratification is quite weak ( $N \approx 0.004 \text{ s}^{-1}$ ) and a potentially unstable layer is present by enhanced humidity in the supersaturated layer. During the simulation, convective activity leads to transport of the latent heat and mixing. At simulation time  $t = 360$  min, the potential temperature profile has changed over the whole layer. In the upper part ( $z \geq 9$  km) stability has decreased, whereas

in the lower part ( $z \leq 9$  km) stability has increased. The equivalent potential temperature approaches neutral stratification, but a slight potentially unstable layer remains. Thus, convective mixing is not strong enough to remove potential instability completely. Further latent heat release would trigger again (weak) convection. We have calculated a ‘moist-adiabatic’ lapse rate for vapour-ice transitions, similarly to the usual definition of moist-adiabatic lapse-rates (see, e.g., Emanuel, 1994). However, the final profile does not approach this ‘moist-adiabatic’ lapse-rate, even not for a constant supersaturation  $S_i \neq 1$ . Thus, for shallow convection in pure ice clouds there is not a final state in mixing reaching ‘moist-adiabatic’ lapse-rate, that is, a state near thermodynamic equilibrium. This is in contrast to the usual behaviour for pure liquid convective clouds. Since thermodynamic equilibrium is not a typical state for ice clouds in contrast to liquid clouds, this is not a surprising result.

3.3.6. Comparison of radiosonde profiles with ‘pseudo-radiosoundings’. In our realistic case, there are no *in situ* measurements of ice crystals for corroborating the

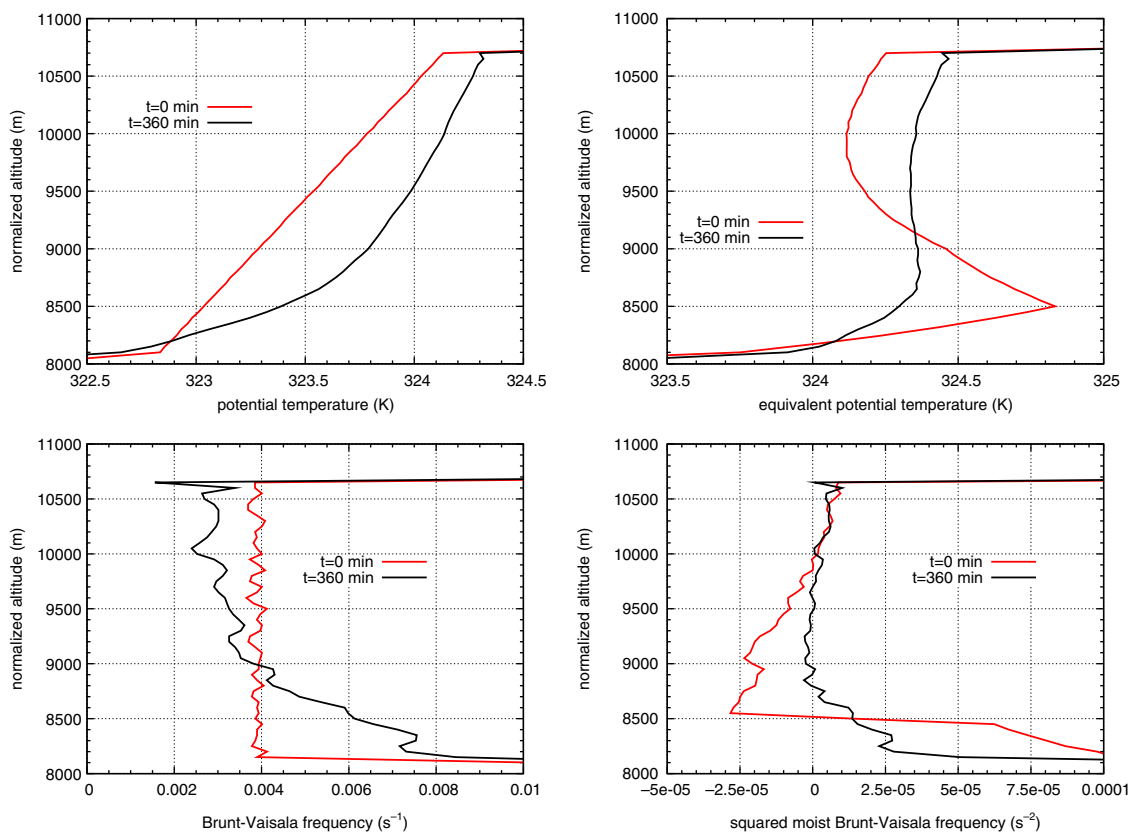


Fig. 18. Vertical profiles of potential temperature, entropy ice potential temperature, Brunt-Vaisala frequency and squared moist Brunt-Vaisala frequency, respectively, at times  $t = 0$  min and  $t = 360$  min, shifted to an equivalent height (i.e. start height).

existence of convective cells; therefore, we have to carry out a circumstantial evidence. For this purpose we compare the vertical profile of potential temperature as measured by the radiosonde with several ‘pseudo-radiosonde’ profiles. For a horizontal grid point we extract the vertical column at this point as a ‘pseudo-radiosonde’ ascent. The realisations are given for a distinct simulation time ( $t = 195$  min) equivalent to the realistic radiosonde ascent.

The measured profile of potential temperature (Fig. 19, thick line) shows a high variability. Some unstable layers are embedded into stable layers. The perturbations in potential temperature are in the order of  $\Delta\theta \sim 0.2\text{--}0.5$  K. As we have seen from our investigation of a single convective cell, such perturbations might result from an ascending convective cell. Temperature perturbations from latent heat release are transported upwards by the updraught of the cell, leading to a signature of an unstable layer. We see a similar signature in the pseudo-radiosondes as extracted from the model simulation. Figure 19 shows eight realisations of vertical profiles, shifted by  $\Delta\theta = 0.5$  K for better representation. We cannot expect that the realistic profile is represented in a 1–1 relation. However, many profiles show very similar structures as in the observations; the magnitude of simulated perturbations is in very good agreement with measured perturbations. Thus, this is a strong indication that the structure in the radiosonde profile of potential temperature is crucially determined by convective cells in cirrus clouds.

#### 4. Discussion

The key for ice supersaturation inside cirrus clouds is a source term due to vertical updraughts. Timescale analysis showed clearly that this cooling term in relative humidity rates is almost always dominating over other terms. Although latent heat release and in turn formation of

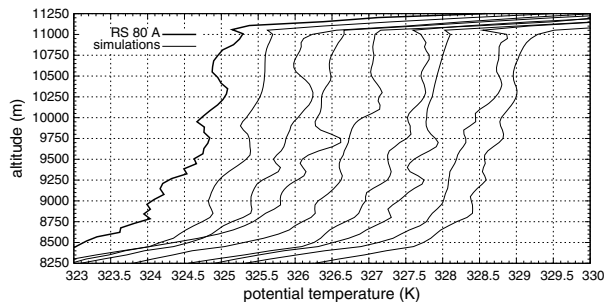


Fig. 19. Potential temperature profile as obtained from the radiosonde (thick line) and eight realisations from the simulation at a corresponding simulation time ( $t = 195$  min). The profiles are shifted by  $\Delta\theta = 0.5$  K for a better representation.

cellular structures is the dominant effect for ice supersaturation inside cirrus clouds in this study, some other effects might influence or modify this feature. Here we discuss some other effects:

- Impact of radiation:

In our simulations we omit radiative transfer calculations with feedbacks to the cloud dynamics. This was done for concentrating on feedbacks of latent heat release only. Cloud-radiation feedbacks are very complex processes and depend on many environmental conditions. Ice crystals absorb solar radiation and the high water vapour inside the clouds lead to a strong signal in infrared radiation. In turn, cirrus clouds produce local heating rates. The exact values depend strongly on environmental conditions. Therefore, we decided to leave out the effect. We have carried out off-line radiative transfer calculations in order to estimate typical heating rates inside the cells. For this purpose we used the radiative transfer code by Fu and Liou (1993) and adapted formulae for the effective size of the ice crystals (see Appendix in Joos et al., 2014). For typical mid-latitude conditions in spring (latitude  $\sim 50^\circ$ , surface temperature  $T_s \sim 300$  K) we could derive local heating rates in order of  $\frac{dT}{dt} \sim 10 \text{ K day}^{-1} \sim 10^{-4} \text{ K s}^{-1}$ . These maximum values are of similar order of magnitude as latent heating rates. Since the absorption of radiation is proportional to ice mass concentration, the maximum values occur at high values of IWC inside convective cells. By this coincidence, one can conclude that radiation would simply enhance the vertical upward motions due to additional heating inside the cells. Gu and Liou (2000) found similar behaviour. Thus, the qualitative structure of shallow cirrus convection will not change including radiation but the analysis of the data might be more complicated. The impact of radiation is limited by the life time of the cells, as in case of latent heating.

- Additional heterogeneous nucleation:

The dominant ice formation process in the extra tropical tropopause region is homogeneous freezing of aqueous solution droplets (Kärcher and Ström, 2003). Heterogeneous nucleation might play a minor role. For the sub tropics, the picture might change, as recent studies suggest; this is probably due to the high loading of heterogeneous IN in the subtropical upper troposphere (Cziczo et al., 2013). Boxmodel studies without including sedimentation proposed suppression of homogeneous nucleation

for small number concentrations of IN in order of  $N_{IN} \sim 10 \text{ L}^{-1}$  (Gierens, 2003; Ren and MacKenzie, 2005). If sedimentation is included, box model studies suggest more a modification of homogeneous nucleation events for typical IN concentrations in the tropopause region (Haag and Kärcher, 2004; Spichtinger and Cziczo, 2010). In former studies using LES models, perturbation and modification of homogeneous nucleation by heterogeneous IN was corroborated (Spichtinger and Gierens, 2009c; Joos et al., 2014). For investigating the impact of heterogeneous IN on shallow cirrus convection, we run the model including heterogeneous IN with a nucleation threshold at  $RH_{IN,thres} = 130\%$  and a number concentration of  $N_{IN} = 10 \text{ L}^{-1}$  as described in Section 3.2. The results show no qualitative difference in the convective cell activity. In case of additional heterogeneous IN, convective activity was triggered earlier due to the lower nucleation threshold compared to homogeneous nucleation. The main structure of convective cells as well as of high supersaturation inside the cells remains the same. Ice supersaturation is present in the cells as for pure homogeneous nucleation. We do not quantify the impact of heterogeneous nucleation further, because this is beyond the scope of this study. In an upcoming study, we will address this issue in a more idealised setup.

- Role of sedimentation:

Sedimentation of ice crystals due to gravity is of high importance for the development of cirrus clouds (see, e.g., Spichtinger and Gierens, 2009c; Spichtinger and Cziczo, 2010). In box model studies this effect is usually neglected, although some models deal with rudimental sedimentation approaches (Haag and Kärcher, 2004; Kay et al., 2006; Spichtinger and Cziczo, 2010). As discussed above, fall streaks are formed by sedimentation. The removal of ice crystals from their origin by gravity leads to a weakening of the growth term in the relative humidity rate [eq. (3)]. This results into less latent heat release, which feedbacks to vertical velocity. We tested the impact of sedimentation by running a simulation without sedimentation. As expected, the ice crystals stay in the cells; they can only be removed by active warming of the cells due to downdraughts. Convective activity starts earlier since latent heat release is more effective at the beginning. However, the initial structure of the cells remains similarly to the standard run. The overturning of the cells is enhanced; the verti-

cal velocities do not change as compared to the reference simulation. The ice water content is about 2–5 times higher but ice crystal number concentrations are somewhat reduced due to very efficient quenching. In contrast to the standard run with spacings between the cells in order of some kilometres, in the sensitivity run the whole 2D domain is filled with clouds after about 180 min. Although one would think that growth should be more effective, the timescale analysis shows that still the velocity driven source of supersaturation dominates overall other terms. High ice supersaturation is still possible and frequent. The strong internal overturning leads to subsidence regions with warming and sublimation of the ice crystals. Additionally, water vapour and ice mass concentrations are spread by mixing.

## 5. Summary and conclusions

We investigated the hypothesis of shallow convection inside cirrus clouds (‘shallow cirrus convection’) in the tropopause region. Measurements from radiosondes and ECMWF meteorological analyses show evidence of a potentially unstable layer in the upper troposphere with a large vertical extension in order of 2 km. We used a state-of-the-art large-eddy cirrus simulation model for simulating this realistic case. From the simulations, we could derive the following main results.

- (1) Shallow cirrus convection is possible in analogy to classical cloud dynamics for liquid clouds. A potentially unstable layer is externally lifted by large-scale motion, leading to first ice nucleation events. Cell formation is triggered by latent heat release of growing ice crystals. During the developing stage, sedimenting ice crystals form characteristic fall streaks. The cells rise until they reach their level of neutral buoyancy near the tropopause. Then they decay and evaporate in the subsidence around the updraught regions of the cells.
- (2) Ice supersaturation inside cirrus clouds can be triggered by shallow cirrus convection. The source for supersaturation is the intrinsic updraught of convective cells, leading to cooling and increase of relative humidity. The source term driven by vertical velocity is almost always dominating over sinks in supersaturation, given by diffusional growth. The same is true for subsidence regions. Also in such cases, drying of air in terms of relative humidity due to downward motion dominates over possible moistening due to sublimating ice crystals.

- (3) Mixing due to local dynamics can also influence relative humidity in cirrus clouds. Timescale analysis for relative humidity rates shows that the impact of mixing is usually small compared to cooling, but could be of same order as diffusional growth.
- (4) Cirrus clouds in shallow cirrus convection are usually not in thermodynamic equilibrium (i.e. saturation). Just about 11.5% of all cloudy data ( $N_i \geq N_{i,theres} = 1 \text{ L}^{-1}$ ) are close to saturation. About 52% of cloudy data are found at ice supersaturation, whereas about 36.5% of cloudy data are found in subsaturated air. Since cirrus clouds constitute an open thermodynamic system, this result is consistent with non-equilibrium thermodynamics.
- (5) About 14% of all cloudy data represent thick cirrus clouds ( $\text{IWC} \geq 10 \text{ mg m}^{-3}$ ) in status of ice supersaturation. Even for very thick cirrus clouds ( $\text{IWC} \geq 30 \text{ mg m}^{-3}$ ), ice supersaturation is possible (which occurs in about 1.7% of all cloudy data). High supersaturation ( $S_i \geq 12$ ) inside cirrus clouds could be found in about 20% of all cloudy data, very high supersaturation ( $S_i \geq 14$ ) is present in about 5% of all cloud events (see also values reported in Table 1)
- (6) Relative humidity probability density functions show exponential decay in the supersaturated interval for clear and cloudy air conditions, mostly during the later stage of the convection evolution. This is in contrast to our former conjecture that the exponential feature is dominant for clear measurements only. The exponential feature is probably driven by strong mixing inside the cirrus layer.
- (7) Sedimentation is an important process for shaping cells in the manner of fall streaks. Diffusional growth and sedimentation are of equal importance in terms of timescale analysis. High variations in the dominance can occur (i.e.  $|\tau_{dep}| < |\tau_{sed}|$  and  $|\tau_{dep}| > |\tau_{sed}|$ ). Mixing does also influence ice cloud mixing ratios; however, sedimentation is always dominating in comparison to mixing.
- (8) The rising cells transport potential temperature, ice and water vapour into the upper part of the layer; the subsidence around the cells transport upper air masses downwards. These effects lead to a general kind of mixing, driven by the life cycle of the cells. At the end of the simulations a partly mixed layer was established; however, the layer includes still some potentially unstable parts. The final stratification differs from moist-adiabatic lapse rate. Therefore we conclude that shallow cirrus convection does not generally lead to a well-mixed state. This is due to the very moderate updraughts in the range  $|w| \leq 1.5 \text{ m s}^{-1}$ , driven by small latent heat release from small water vapour mixing ratios.

- (9) Ice supersaturation in shallow cirrus convection is a transient phenomenon. It is not persistent but is limited to the lifetime of convective cells. This feature can only be detected introducing time-dependent investigations.

We were able to investigate shallow cirrus convection and derived some results corroborating the existence of high ice supersaturation inside cirrus clouds, as driven by vertical motions. Dynamics is the key for the multi scale system of cirrus clouds in their environment. From our investigation we can carefully conclude that dynamics is the dominating process driving thermodynamic states of cirrus clouds. Microphysical effects might modify cirrus cloud processes. Probably, in many cases of actual measurements superposition of dynamics on different scales might explain thermodynamic conditions (see also Spichtinger and Krämer, 2013). Our investigations are representative in absence of additional motions, which could superimpose large-scale dynamics and convective cell dynamics. For instance, gravity waves propagating through cirrus layers might change the qualitative results. However, small-scale variability is represented in the simulations in form of initially prescribed perturbations of potential temperature. Additional turbulence would be related to breaking waves, which are excluded in our case.

Finally, we want to remark that the origin of the potentially unstable layer in our case is not clear. Possible formation mechanisms are large-scale advection and mixing of different air masses, mesoscale mixing processes (e.g. near the jet regions due to strong wind shear) or radiation processes in cloudy and clear air with an enhanced water vapour content (leading to strong radiative cooling). In future work, these issues should be clarified. In future studies, we will investigate the impact of environmental conditions on shallow cirrus convection in more detail.

## 6. Acknowledgements

I thank Ulrich Achatz, Marcia Baker, Andreas Dörnbrack, Fabian Fusina, Hanna Joos, Ulrich Schumann, Piotr Smolarkiewicz and Heini Wernli for fruitful discussions. I also thank two anonymous reviewers; their comments helped to improve the manuscript significantly. This work was partly supported by the European Commission within the framework of a Marie Curie fellowship (Impact of mesoscale dynamics and aerosols on the life cycle of cirrus clouds). This work contributes to the COST action ‘Water Vapour in the Climate System’ (WaVaCS). The simulations were carried out on the high-performance computing facilities of the European Centre for Medium-Range Forecasts (ECMWF) within the framework of the special project ‘Ice supersaturation and cirrus clouds’ (SPDEISSR).



## 7. Appendix: derivation of timescales

The general assumption for timescale analysis of a quantity  $\psi$ , driven by several competing processes  $i = 1, \dots, n$  is as follows:

$$\frac{d\psi}{dt} \stackrel{!}{=} \frac{\psi}{\tau_1} + \dots + \frac{\psi}{\tau_n} \quad (9)$$

that is, each process  $i$  is linked to an instantaneous timescale  $\tau_i$ , which would result into an exponential behaviour. For the superposition of the different processes  $i = 1, \dots, n$ , we can write

$$\psi(t) = \sum_{i=1}^n \exp\left(\frac{t}{\tau_i}\right) \quad (10)$$

By definition, timescales can have different signs, indicating sources and sinks for the quantity  $\psi$ . For the investigations in shallow cirrus convection, that is, in the cells, two different variables must be studied, relative humidity over ice (or equivalently the saturation ratio  $S_i = RH_i/100\%$ ) and ice mass mixing ratio. For this purpose, we derive the following equations:

- (1) Relative humidity evolution:  $RHi$  depends on temperature, pressure and water vapour mixing ratio, respectively. Thus, we have to consider changes in these variables, given by external forcings (vertical motion and mixing) and phase transitions in the system. Mixing plays a minor role for temperature and pressure changes, since the horizontal and vertical gradients on grid resolution are small and also variations are quite small; therefore mixing can be neglected for temperature and pressure. The temperature, pressure and humidity rates can be described as follows:

$$\begin{aligned} \frac{dT}{dt} &= \frac{dT}{dt}|_{\text{vertical}} + \frac{dT}{dt}|_{\text{mixing}} + \frac{dT}{dt}|_{\text{phase}} \\ &\approx \frac{dT}{dt}|_{\text{vertical}} + \frac{dT}{dt}|_{\text{phase}} \end{aligned} \quad (11)$$

$$\frac{dp}{dt} = \frac{dp}{dt}|_{\text{vertical}} + \frac{dp}{dt}|_{\text{mixing}} \approx \frac{dp}{dt}|_{\text{vertical}} \quad (12)$$

$$\frac{dq}{dt} = \frac{dq}{dt}|_{\text{mixing}} + \frac{dq}{dt}|_{\text{phase}} \quad (13)$$

For the changes of temperature we get the following equations

$$\frac{dT}{dt}|_{\text{vertical}} = -\frac{g}{c_p} w, \quad \frac{dT}{dt}|_{\text{phase}} = -\frac{L_s}{c_p} \frac{dq}{dt}|_{\text{phase}}, \quad (14)$$

whereas for pressure we can express the changes via temperature changes

$$\frac{dp}{dt}|_{\text{vertical}} = \frac{1}{\kappa} \frac{p}{T} \frac{dT}{dt}|_{\text{vertical}} = -\frac{g}{c_p} w \frac{1}{\kappa} \frac{p}{T} \quad (15)$$

For diagnosing mixing, we make an ansatz in terms of eddy diffusivity, that is, the changes in concentrations due to mixing can be described by the following equation.

$$\frac{dq}{dt}|_{\text{mixing}} = \nabla \cdot (K_q \nabla q) = \frac{\partial}{\partial x} K_q \frac{\partial q}{\partial x} + \frac{\partial}{\partial z} K_q \frac{\partial q}{\partial z} \quad (16)$$

$K_q$  denotes the eddy diffusivity coefficient, related to turbulent kinetic energy  $E$

$$E = \frac{1}{2} (u'^2 + w'^2), \quad u' = u - u_e, \quad w' = w - w_{LS} \quad (17)$$

The perturbation velocities are given by subtracting the initial horizontal wind profile  $u_e(z)$  as represented in Fig. 7 (left panel) and subtracting the large-scale vertical wind component. The diffusivity can be expressed by  $K_q := c \cdot \ell \cdot \sqrt{E}$  with the characteristic length scale of grid resolution  $\ell = \sqrt{\Delta x \cdot \Delta z} \approx 71$  m and a constant  $c = 0.2$  (see, e.g., Schumann, 1991; Grabowski, 2007). Using the expressions for partial derivatives

$$\frac{\partial RH_i}{\partial T} = -RH_i \frac{L_s}{R_v T^2}, \quad \frac{\partial RH_i}{\partial p} = \frac{RH_i}{p}, \quad \frac{\partial RH_i}{\partial q} = \frac{RH_i}{q} \quad (18)$$

we end with an equation for sources and sinks of relative humidity:

$$\begin{aligned} \frac{dRH_i}{dt} &= \underbrace{\frac{RH_i}{T} \left[ \frac{L_s}{R_v T} - \frac{1}{\kappa} \right] \cdot \frac{g}{c_p} w}_{\text{vertical velocity}} + \underbrace{RH_i \left[ \frac{L_s}{R_v T^2 c_p} + \frac{1}{q} \right] \frac{dq}{dt}|_{\text{phase}}}_{\text{phase change}} \\ &\quad + \underbrace{\frac{RH_i}{q} \nabla \cdot (K_q \nabla q)}_{\text{mixing}} \end{aligned} \quad (19)$$

Using the growth equation for the specific humidity rate, that is,

$$\frac{dq}{dt}|_{\text{phase}} = -\frac{dq_c}{dt} = -a \cdot N^{1-b} q_c^b r_b \quad (20)$$

whereas  $a = f \cdot a^*(p, T)$ ,  $b = b(p, T)$ ,

$$f = \frac{p_v - p_{ice}(T)}{p_{liq}(T) - p_{ice}(T)}, \quad r_b := \exp\left(\frac{b(b-1)}{2} (\log \sigma_m)^2\right) \quad (21)$$

and  $\sigma_m$  denotes the geometric width of the lognormal mass distribution. The coefficients  $a^*$ ,  $b$  are described by

Spichtinger and Gierens (2009a). The final expression for the relative humidity rate is then as follows:

$$\begin{aligned} \frac{dRH_i}{dt} &= \underbrace{\frac{RH_i}{T} \left[ \frac{L_s}{R_v T} - \frac{1}{\kappa} \right] \cdot \frac{g}{c_p} w}_{\text{vertical=cooling}} \\ &\quad - \underbrace{RH_i \left[ \frac{L_s^2}{R_v T^2 c_p} + \frac{1}{q} \right] \cdot a \cdot N^{1-b} q_c^b r_b}_{\text{phase change}} \quad (22) \\ &\quad + \underbrace{\frac{RH_i}{q} \nabla \cdot (K_q \nabla q)}_{\text{mixing}} \\ &\stackrel{!}{=} \frac{RH_i}{\tau_{cool}} + \frac{RH_i}{\tau_{phase}} + \frac{RH_i}{\tau_{mix,RHi}} \quad (23) \end{aligned}$$

Since, we mostly investigate upward motions, we adopt the usual term for the vertical forcing to be ‘cooling’. The timescales for cooling, phase change and mixing, respectively, are given by

$$\tau_{cool} = \left[ \frac{1}{T} \left[ \frac{L_s}{R_v T} - \frac{1}{\kappa} \right] \cdot \frac{g}{c_p} w \right]^{-1} \quad (24)$$

$$\tau_{phase} = \left[ - \left[ \frac{L_s^2}{R_v T^2 c_p} + \frac{1}{q} \right]^{1-b} q_c^b r_b \right]^{-1} \quad (25)$$

$$\tau_{mix,RHi} = \frac{q}{\nabla \cdot (K_q \nabla q)} \quad (26)$$

- (2) Cloud ice mixing ratio evolution: Cloud ice mass is changed by growth by diffusion, sedimentation and mixing due to eddies. For mixing, we use the same ansatz as above, but now for cloud ice mass concentration  $q_c$ . Thus, the rate equation can be described as

$$\frac{dq_c}{dt} = \frac{dq_c}{dt} \Big|_{growth} + \frac{dq_c}{dt} \Big|_{sed} + \frac{dq_c}{dt} \Big|_{mixing} \quad (27)$$

$$= a \cdot N^{1-b} q_c^b r_b + \frac{1}{\rho} \frac{\partial(\rho \bar{v}_{q_c} q_c)}{\partial z} + \nabla \cdot (K_{q_c} \nabla q_c) \quad (28)$$

$$\stackrel{!}{=} \frac{q_c}{\tau_{growth}} + \frac{q_c}{\tau_{sed}} + \frac{q_c}{\tau_{mix,q_c}} \quad (29)$$

while  $\frac{dq_c}{dt} \Big|_{phase} = -\frac{dq_c}{dt} \Big|_{growth}$ . Note, that because  $q, q_c$  are scalars, we can set  $K_q = K_{q_c}$  (Schumann, 1991). Thus, we can define timescales for the ice mass mixing ratio

$$\tau_{growth} = \left[ a \cdot N^{1-b} q_c^{b-1} r_b \right]^{-1} \quad (30)$$

$$\tau_{sed} = \rho q_c \left[ \frac{\partial(\rho \bar{v}_{q_c} q_c)}{\partial z} \right]^{-1} \quad (31)$$

$$\tau_{mix,q_c} = \frac{q_c}{\nabla \cdot (K_{q_c} \nabla q_c)} \quad (32)$$

Note, that timescales  $\tau_{growth}$  and  $\tau_{phase}$  are different, although they rely to the same process (phase change due to diffusional growth).

## References

- Bogdan, A. and Molina, M. J. 2009. Why does large relative humidity with respect to ice persist in cirrus ice clouds? *J. Phys. Chem.* **113**, 14123–14130.
- Brabec, M., Wienhold, F. G., Luo, B. P., Vmel, H., Immler, F. and co-authors. 2013. Particle backscatter and relative humidity measured across cirrus clouds and comparison with microphysical cirrus modelling. *Atmos. Chem. Phys.* **12**, 9135–9148. DOI: 10.5194/acp-12-9135-2012.
- Bretherton, C. S. and Smolarkiewicz, P. K. 1989. Gravity waves, compensating subsidence and detrainment around cumulus clouds. *J. Atmos. Sci.* **46**, 740–759.
- Cirisan, A., Luo, B. P., Engel, I., Wienhold, F. G., Krieger, U. K. and co-authors. 2014. Balloon-borne match measurements of mid-latitude cirrus clouds. *Atmos. Chem. Phys.* **14**, 7341–7365.
- Cirisan, A., Spichtinger, P., Luo, B. P., Weisenstein, D. K., Wernli, H. and co-authors. 2013. Microphysical and radiative changes in cirrus clouds by geoengineering the stratosphere. *J. Geophys. Res.* **118**, 4533–4548. DOI: 10.1002/jgrd.50388.
- Chen, T., Rossow, W. B. and Zhang, Y. 2000. Radiative effects of cloud-type variations. *J. Clim.* **13**, 264–286.
- Comstock, J., Lin, R.-F., Starr, D. O. and Yang, P. 2008. Understanding ice supersaturation, particle growth, and number concentration in cirrus clouds. *J. Geophys. Res.* **113**, D23211. DOI: 10.1029/2008JD010332.
- Cziczo, D. J., Froyd, K. D., Hoose, C., Jensen, E. J., Diao, M. and co-authors. 2013. Clarifying the dominant sources and mechanisms of cirrus cloud formation. *Science*. **340**, 1320–1324. DOI: 10.1126/science.1234145.
- DeMott, P., Cziczo, D., Prenni, A., Murphy, D., Kreidenweis, S. and co-authors. 2003. Measurements of the concentration and composition of nuclei for cirrus formation. *Proc. Natl. Acad. Sci. U. S. A.* **100**, 14655–14660.
- Emanuel, K. A. 1994. *Atmospheric Convection*. Oxford University Press, New York.
- Fahey, D. W., Gao, R.-S., Möhler, O., Saathoff, H., Schiller, C. and co-authors. 2014. The AquaVIT-1 intercomparison of atmospheric water vapor measurement techniques. *Atmos. Meas. Tech. Discuss.* **7**, 3159–3251.
- Fu, Q. and Liou, K. 1993. Parameterization of the radiative properties of cirrus clouds. *J. Atmos. Sci.* **50**, 2008–2025. DOI: 10.1175/1520-0469(1993)050 <2008:POTRPO>2.0.CO;2.
- Fusina, F. and Spichtinger, P. 2010. Cirrus clouds triggered by radiation, a multiscale phenomenon. *Atmos. Chem. Phys.* **10**, 5179–5190. DOI: 10.5194/acp-10-5179-2010.
- Fusina, F., Spichtinger, P. and Lohmann, U. 2007. The impact of ice supersaturated regions and thin cirrus on radiation in the mid latitudes. *J. Geophys. Res.* **112**, D24S14. DOI: 10.1029/2007JD008449.
- Gary, B. L. 2006. Mesoscale temperature fluctuations in the stratosphere. *Atmos. Chem. Phys.* **6**, 4577–4589.

- Gensch, J., Bunz, H., Baumgardner, D. G., Christensen, L. E., Fahey, D. W. and co-authors. 2008. Supersaturations, microphysics and nitric acid partitioning in a cold cirrus cloud observed during CR-AVE 2006: an observation-modelling intercomparison study. *Environ. Res. Lett.* **3**, 035003. DOI: 10.1088/1748-9326/3/3/035003.
- Gettelman, A., Fetzer, E. J., Eldering, A. and Irion, F. W. 2006. The global distribution of supersaturation in the upper troposphere from the Atmospheric Infrared Sounder. *J. Clim.* **19**, 6089–6103.
- Gierens, K. 2003. On the transition between heterogeneous and homogeneous freezing. *Atmos. Chem. Phys.* **3**, 437–446.
- Gierens, K., Kohlhepp, R., Dotzek, N. and Smit, H. 2007. Instantaneous fluctuations of temperature and moisture in the upper troposphere and tropopause region. Part 1: probability densities and their variability. *Meteorol. Z.* **16**, 221–231.
- Gierens, K., Kohlhepp, R., Spichtinger, P. and Schroedter-Homscheidt, M. 2004. Ice supersaturation as seen from TOVS. *Atmos. Chem. Phys.* **4**, 539–547.
- Gierens, K., Schumann, U., Helten, M., Smit, H. and Marenco, A. 1999. A distribution law for relative humidity in the upper troposphere and lower stratosphere derived from three years of MOZAIC measurements. *Ann. Geophys.* **17**, 1218–1226.
- Gierens, K. and Spichtinger, P. 2000. On the size distribution of ice supersaturation regions in the upper troposphere and lower stratosphere. *Ann. Geophys.* **18**, 499–504.
- Grabowski, W. W. 2007. Representation of turbulent mixing and buoyancy reversal in bulk cloud models. *J. Atmos. Sci.* **64**, 3666–3680.
- Gu, Y. and Liou, K. N. 2000. Interactions of radiation, microphysics, and turbulence in the evolution of cirrus clouds. *J. Atmos. Sci.* **57**, 2463–2479.
- Haag, W. and Kärcher, B. 2004. The impact of aerosols and gravity waves on cirrus clouds at midlatitudes. *J. Geophys. Res.* **109**, D12202. DOI: 10.1029/2004JD00457.
- Haag, W., Kärcher, B., Strm, J., Minikin, A., Lohmann, U. and co-authors. 2003. Freezing thresholds and cirrus cloud formation mechanisms inferred from in situ measurements of relative humidity. *Atmos. Chem. Phys.* **3**, 1791–1806.
- Houze, R. A. 1993. *Cloud Dynamics*. Academic Press, San Diego, 573 pp.
- Hoyle, C., Luo, B. and Peter, T. 2005. The origin of high ice crystal number densities in cirrus clouds. *J. Atmos. Sci.* **62**, 2568–2579.
- Jensen, E. J., Toon, O. B., Tabazadeh, A., Sachse, G. W., Anderson, B. E. and co-authors. 1998. Ice nucleation processes in upper tropospheric wave-clouds observed during SUCCESS. *Geophys. Res. Lett.* **25**, 1363.
- Joos, H., Spichtinger, P. and Lohmann, U. 2009. Orographic cirrus in a future climate. *Atmos. Chem. Phys.* **9**, 7825–7845.
- Joos, H., Spichtinger, P., Lohmann, U., Gayet, J.-F. and Minikin, A. 2008. Orographic cirrus in the global climate model ECHAM5. *J. Geophys. Res.* **113**, D18205. DOI: 10.1029/2007JD009605.
- Joos, H., Spichtinger, P., Reutter, P. and Fusina, F. 2014. Influence of heterogeneous freezing on the microphysical and radiative properties of orographic cirrus clouds. *Atmos. Chem. Phys.* **14**, 6835–6852. DOI: 10.5194/acp-14-6835-2014.
- Kajikawa, M. and Heymsfield, A. 1989. Aggregation of ice crystals. *J. Atmos. Sci.* **46**, 3108–3121.
- Kärcher, B. and Koop, T. 2005. The role of organic aerosols in homogeneous ice formation. *Atmos. Chem. Phys.* **5**, 703–714.
- Kärcher, B. and Lohmann, U. 2002. A parameterization of cirrus cloud formation: homogeneous freezing of supercooled aerosols. *J. Geophys. Res.* **107**(D2), 4010. DOI: 10.1029/2001JD000470.
- Kärcher, B. and Ström, J. 2003. The roles of dynamical variability and aerosols in cirrus cloud formation. *Atmos. Chem. Phys.* **3**, 823–838.
- Kay, J. and Wood, R. 2008. Timescale analysis of aerosol sensitivity during homogeneous freezing and implications for upper tropospheric water vapor budgets. *Geophys. Res. Lett.* **35**, L10809. DOI: 10.1029/2007GL032628.
- Kay, J. E., Baker, M. and Hegg, D. 2006. Microphysical and dynamical controls on cloud optical depth distributions. *J. Geophys. Res.* **111**, D24205. DOI: 10.1029/2005JD006916.
- Kay, J. E., Baker, M. and Hegg, D. 2007. Physical controls on orographic cirrus inhomogeneity. *Atmos. Chem. Phys.* **7**, 3771–3781.
- Klein, R. and Majda, A. 2006. Systematic multiscale models for deep convection on mesoscales. *Theor. Comp. Fluid Dyn.* **20**, 525–552.
- Koop, T., Bookhold, J., Shiraiwa, M. and Pöschl, U. 2011. Glass transition and phase state of organic compounds: dependency on molecular properties and implications for secondary organic aerosols in the atmosphere. *Phys. Chem. Chem. Phys.* **13**, 19238–19255.
- Koop, T., Luo, B., Tsias, A. and Peter, T. 2000. Water activity as the determinant for homogeneous ice nucleation in aqueous solutions. *Nature*. **406**, 611–614.
- Korolev, A. and Mazin, I. 2003. Supersaturation of water vapor in clouds. *J. Atmos. Sci.* **60**, 2957–2974.
- Krämer, M., Schiller, C., Afchine, A., Bauer, R., Gensch, I. and co-authors. 2009. On cirrus cloud supersaturations and ice crystal numbers. *Atmos. Chem. Phys.* **9**, 3505–3522.
- Lane, T. P., Doyle, J. D., Plougonven, R., Shapiro, M. A. and Sharman, R. D. 2004. Observations and numerical simulations of inertia-gravity waves and shearing instabilities in the vicinity of a jet stream. *J. Atmos. Sci.* **61**, 2692–2706.
- Lane, T. P., Reeder, M. J. and Clark, T. L. 2001. Numerical modeling of gravity wave generation by deep tropical convection. *J. Atmos. Sci.* **58**, 1249–1274.
- Lee, S.-H., Wilson, J. C., Baumgardner, D., Herman, R. L., Weinstock, E. M. and co-authors. 2004. New particle formation observed in the tropical/subtropical cirrus clouds. *J. Geophys. Res.* **109**, D20209. DOI: 10.1029/2004JD005033.
- Leiterer, U., Dier, H., Nagel, D., Naebert, T., Althausen, D. and co-authors. 2005. Correction method for RS80-A Humicap humidity profiles and their validation by lidar backscattering profiles in tropical cirrus clouds. *J. Atmos. Ocean. Tech.* **22**, 18–29.
- Lin, Y.-L. 2008. *Mesoscale Dynamics*. Cambridge University Press, Cambridge, UK, 646 pp.

- Lott, F., Kelder, H. and Teitelbaum, H. 1992. A transition from Kelvin-Helmholtz instabilities to propagating wave instabilities. *Phys. Fluids A*, **4**, 1990. DOI: 10.1063/1.858368.
- Marshall, J. H. and Dobbie, S. 2005. The effects of wind shear on cirrus: a large-eddy model and radar case-study. *Q. J. Roy. Meteorol. Soc.* **131**, 2937–2955.
- McIntyre, M. E. 2008. Potential-vorticity inversion and the wave-turbulence jigsaw: some recent clarifications. *Adv. Geosci.* **15**, 47–56.
- Minikin, A., Petzold, A., Ström, J., Krejci, R., Seifert, M. and co-authors. 2003. Aircraft observations of the upper tropospheric fine particle aerosol in the Northern and Southern Hemispheres at midlatitudes. *Geophys. Res. Lett.* **30**, 1503. DOI: 10.1029/2002GL016458.
- Murphy, D. M. 2003. Dehydration in cold clouds is enhanced by a transition from cubic to hexagonal ice. *Geophys. Res. Lett.* **30**, 2230.
- Murphy, D. M. and Koop, T. 2005. Review of the vapour pressure of ice and supercooled water for atmospheric applications. *Q. J. Roy. Meteorol. Soc.* **131**, 1539–1565.
- Murray, B. J. 2008a. Inhibition of ice crystallisation in highly viscous aqueous organic acid droplets. *Atmos. Chem. Phys.* **8**, 5423–5433.
- Murray, B. J. 2008b. Enhanced formation of cubic ice in aqueous organic acid droplets. *Environ. Res. Lett.* **3**, 025008. DOI: 10.1088/1748-9326/3/2/025008.
- Murray, B. J., Knopf, D. A. and Bertram, A. K. 2005. The formation of cubic ice under conditions relevant to Earth's atmosphere. *Nature*, **434**, 202–205.
- Murray, B. J., Wilson, T. W., Dobbie, S., Cui, Z., Al-Jumur, S. M. R. K. and co-authors. 2010. Heterogeneous nucleation of ice particles on glassy aerosols under cirrus conditions. *Nat. Geosci.* **3**, 233–237.
- O'Sullivan, D. and Dunkerton, T. 1995. Generation of inertia-gravity waves in a simulated life cycle of baroclinic instability. *J. Atmos. Sci.* **52**, 3695–3716.
- Ovarlez, J., van Velthoven, P., Sachse, G., Vay, S., Schlager, H. and co-authors. 2000. Comparison of water vapor measurements from POLINAT 2 with ECMWF analyses in high humidity conditions. *J. Geophys. Res.* **105**(D3), 3737–3744.
- Peter, T., Marcolli, C., Spichtinger, P., Corti, T., Baker, M. B. and co-authors. 2006. When dry air is too humid. *Science*, **314**(5804), 1399–1402.
- Plougonven, R., Muraki, D. J. and Snyder, C. 2005. A baroclinic instability that couples balanced motions and gravity waves. *J. Atmos. Sci.* **62**, 1545–1559.
- Plougonven, R., Teitelbaum, H. and Zeitlin, V. 2003. Inertia gravity wave generation by the tropospheric midlatitude jet as given by the Fronts and Atlantic Storm-Track Experiment radio soundings. *J. Geophys. Res.* **108**(D21), 4686. DOI: 10.1029/2003JD003535.
- Prusa, J., Smolarkiewicz, P. and Wyszogrodzki, A. 2008. EULAG, a computational model for multiscale flows. *Comput. Fluids*, **37**, 1193–1207.
- Ren, C. and MacKenzie, A. R. 2005. Cirrus parametrization and the role of ice nuclei. *Q. J. Roy. Meteorol. Soc.* **131**, 1585–1605. DOI: 10.1256/qj.04.126.
- Rosenthal, A. J. and Lindzen, R. S. 1983. Instabilities in a stratified fluid having one critical level. Part I: results. *J. Atmos. Sci.* **40**, 509–520.
- Schumann, U. 1991. Subgrid length-scales for large-eddy simulation of stratified turbulence. *Theor. Comput. Fluid Dyn.* **2**, 279–290.
- Shilling, J. E., Tolbert, M. A., Toon, O. B., Jensen, E. J., Murray, B. J. and co-authors. 2006. Measurements of the vapor pressure of cubic ice and their implications for atmospheric ice clouds. *Geophys. Res. Lett.* **33**, L17801. DOI: 10.1029/2006GL026671.
- Skrotzki, J., Connolly, P., Schnaiter, M., Saathoff, H., Mhler, O. and co-authors. 2013. The accommodation coefficient of water molecules on ice – cirrus cloud studies at the AIDA simulation chamber. *Atmos. Chem. Phys.* **13**, 4451–4466. DOI: 10.5194/acp-13-4451-2013.
- Smith, R. 1979. The influence of mountains on the atmosphere. *Adv. Geophys.* **21**, 87–230.
- Smolarkiewicz, P. and Margolin, L. 1997. On forward-in-time differencing for fluids: an Eulerian/Semi-Lagrangian non-hydrostatic model for stratified flows. *Atmos. Oceans*, **35**, 127–152.
- Spichtinger, P. and Cziczo, D. J. 2010. Impact of heterogeneous ice nuclei on homogeneous freezing events in cirrus clouds. *J. Geophys. Res.* **115**, D14208. DOI: 10.1029/2009JD012168.
- Spichtinger, P. and Gierens, K. 2009a. Modelling cirrus clouds. Part 1a: model description and validation. *Atmos. Chem. Phys.* **9**, 685–706.
- Spichtinger, P. and Gierens, K. 2009b. Modelling cirrus clouds. Part 1b: structuring cirrus clouds by dynamics. *Atmos. Chem. Phys.* **9**, 707–719.
- Spichtinger, P. and Gierens, K. 2009c. Modelling cirrus clouds. Part 2: competition of different nucleation mechanisms. *Atmos. Chem. Phys.* **9**, 2319–2334.
- Spichtinger, P., Gierens, K. and Dörnbrack, A. 2005b. Formation of ice supersaturation by mesoscale gravity waves. *Atmos. Chem. Phys.* **5**, 1243–1255.
- Spichtinger, P., Gierens, K., Leiterer, U. and Dier, H. 2003a. Ice supersaturation in the tropopause region over Lindenberg, Germany. *Meteorol. Z.* **12**, 143–156.
- Spichtinger, P., Gierens, K. and Read, W. 2002. The statistical distribution law of relative humidity in the global tropopause region. *Meteorol. Z.* **11**, 83–88.
- Spichtinger, P., Gierens, K. and Read, W. 2003b. The global distribution of ice supersaturated regions as seen by the microwave limb sounder. *Q. J. Roy. Meteorol. Soc.* **129**, 3391–3410.
- Spichtinger, P., Gierens, K., Smit, H. G. J., Ovarlez, J. and Gayet, J.-F. 2004. On the distribution of relative humidity in cirrus clouds. *Atmos. Chem. Phys.* **4**, 639–647.
- Spichtinger, P., Gierens, K. and Wernli, H. 2005a. A case study on the formation and evolution of ice supersaturation in the vicinity of a warm conveyor belt's outflow region. *Atmos. Chem. Phys.* **5**, 973–987.
- Spichtinger, P. and Krämer, M. 2013. Tropical tropopause ice clouds: a dynamical approach to the mystery of low crystal numbers. *Atmos. Chem. Phys.* **13**, 9801–9818. DOI: 10.5194/acp-13-9801-2013.

- Vay, S. A., Anderson, B. E., Jensen, E. J., Sachse, G. W., Ovalez, J. and co-authors. 2000. Tropospheric water vapor measurements over the North Atlantic during the Subsonic Assessment Ozone and Nitrogen Oxide Experiment (SONEX). *J. Geophys. Res.* **105**, 3745–3756.
- Wernli, H. and Davies, H. 1997. A Lagrangian-based analysis of extratropical cyclones. I: the method and some applications. *Q. J. Roy. Meteorol. Soc.* **123**, 467–489.
- Zhang, W., Macke, A. and Albers, F. 1999. Effect of crystal size spectrum and crystal shape on stratiform cirrus radiative forcing. *Atmos. Res.* **52**, 59–79.
- Zobrist, B., Marcolli, C., Pedernera, D. A. and Koop, T. 2008. Do atmospheric aerosols form glasses? *Atmos. Chem. Phys.* **8**, 5221–5244.